



**HAL**  
open science

## Remote Sensing of Air Pollutants in China to Study the Effects of Emission Reduction Policies on Air Quality.

Gerrit de Leeuw, Ronald van der A, Jianhui Bai, Mirjam den Hoed, Jieying Ding, Jianping Guo, Zhengqiang Li, Ying Zhang, Cheng Fan, Kai Qin, et al.

### ► To cite this version:

Gerrit de Leeuw, Ronald van der A, Jianhui Bai, Mirjam den Hoed, Jieying Ding, et al.. Remote Sensing of Air Pollutants in China to Study the Effects of Emission Reduction Policies on Air Quality.. Journal of Atmospheric and Solar-Terrestrial Physics, In press, 10.1016/j.jastp.2024.106392 . hal-04830063

**HAL Id: hal-04830063**

**<https://hal.science/hal-04830063v1>**

Submitted on 10 Dec 2024

**HAL** is a multi-disciplinary open access archive for the deposit and dissemination of scientific research documents, whether they are published or not. The documents may come from teaching and research institutions in France or abroad, or from public or private research centers.

L'archive ouverte pluridisciplinaire **HAL**, est destinée au dépôt et à la diffusion de documents scientifiques de niveau recherche, publiés ou non, émanant des établissements d'enseignement et de recherche français ou étrangers, des laboratoires publics ou privés.

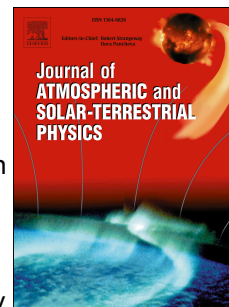


Distributed under a Creative Commons Attribution - NonCommercial - NoDerivatives 4.0 International License

# Journal Pre-proof

Remote Sensing of Air Pollutants in China to Study the Effects of Emission Reduction Policies on Air Quality.

Gerrit de Leeuw, Ronald van der A, Jianhui Bai, Mirjam den Hoed, Jieying Ding, Jianping Guo, Zhengqiang Li, Ying Zhang, Cheng Fan, Kai Qin, Selviga Sinnathamby, Sarah Safieddine, Costas Varotsos, Yong Xue, Yan Yin, Qianqian Zhang, Xin Zhang, XingYing Zhang, Xiumei Zhang



PII: S1364-6826(24)00220-7

DOI: <https://doi.org/10.1016/j.jastp.2024.106392>

Reference: ATP 106392

To appear in: *Journal of Atmospheric and Solar-Terrestrial Physics*

Received Date: 2 July 2024

Revised Date: 3 November 2024

Accepted Date: 30 November 2024

Please cite this article as: de Leeuw, G., van der A, R., Bai, J., den Hoed, M., Ding, J., Guo, J., Li, Z., Zhang, Y., Fan, C., Qin, K., Sinnathamby, S., Safieddine, S., Varotsos, C., Xue, Y., Yin, Y., Zhang, Q., Zhang, X., Zhang, X., Zhang, X., Remote Sensing of Air Pollutants in China to Study the Effects of Emission Reduction Policies on Air Quality., *Journal of Atmospheric and Solar-Terrestrial Physics*, <https://doi.org/10.1016/j.jastp.2024.106392>.

This is a PDF file of an article that has undergone enhancements after acceptance, such as the addition of a cover page and metadata, and formatting for readability, but it is not yet the definitive version of record. This version will undergo additional copyediting, typesetting and review before it is published in its final form, but we are providing this version to give early visibility of the article. Please note that, during the production process, errors may be discovered which could affect the content, and all legal disclaimers that apply to the journal pertain.

© 2024 Published by Elsevier Ltd.

# Remote Sensing of Air Pollutants in China to Study the Effects of Emission Reduction Policies on Air Quality.

Gerrit de Leeuw<sup>1,2,\*</sup>, Ronald van der A<sup>1,3</sup>, Jianhui Bai<sup>4</sup>, Mirjam den Hoed<sup>1</sup>, Jieying Ding<sup>1</sup>, Jianping Guo<sup>5</sup>, Zhengqiang Li<sup>2</sup>, Ying Zhang<sup>2</sup>, Cheng Fan<sup>2</sup>, Kai Qin<sup>6</sup>, Selviga Sinnathamby<sup>7</sup>, Sarah Safieddine<sup>7</sup>, Costas Varotsos<sup>8</sup>, Yong Xue<sup>9</sup>, Yan Yin<sup>3</sup>, Qianqian Zhang<sup>10</sup>, Xin Zhang<sup>3,1,11</sup>, XingYing Zhang<sup>12</sup>, Xiumei Zhang<sup>1,3</sup>

<sup>1</sup>Royal Netherlands Meteorological Institute (KNMI), R&D Satellite Observations, 3731GA De Bilt, The Netherlands

<sup>2</sup>Aerospace Information Research Institute, Chinese Academy of Sciences (AirCAS), No.20 Datun Road, Chaoyang District, Beijing 100101, China

<sup>3</sup>KNMI-NUIST Center for Atmospheric Composition, Nanjing University of Information Science and Technology (NUIST), Nanjing 210044, China

<sup>4</sup>LAGEO, Institute of Atmospheric Physics, Chinese Academy of Sciences (IAP-CAS), Beijing, 100029, China

<sup>5</sup>State Key Laboratory of Severe Weather, Chinese Academy of Meteorological Sciences, Beijing, China

<sup>6</sup>School of Environment Science and Spatial Informatics, China University of Mining and Technology (CUMT), Xuzhou, Jiangsu 221116, China

<sup>7</sup>LATMOS/IPSL, Sorbonne Université, UVSQ, CNRS, Paris, France

<sup>8</sup>Department of Environmental Physics and Meteorology, National and Kapodistrian University of Athens, University Campus, Bldg PHYS-V, GR-157 84 Athens, Greece

<sup>9</sup>School of Computing and Mathematics, College of Science and Engineering, University of Derby, Kedleston Road, Derby DE22 1GB, UK

<sup>10</sup>National Satellite Meteorological Center, China Meteorology Administration, Beijing, 100081, China

<sup>11</sup>Key Laboratory for Aerosol-Cloud-Precipitation of China Meteorological Administration, Nanjing University of Information Science and Technology (NUIST), Nanjing 210044, China

<sup>12</sup>Department of Science & Technology and Climate Change, China Meteorology Administration, Beijing, 100081, China

\*Corresponding author: Gerrit de Leeuw, Royal Netherlands Meteorological Institute (KNMI), R&D Satellite Observations, 3731GA De Bilt, The Netherlands; Email: [gerrit.de.leeuw@knmi.nl](mailto:gerrit.de.leeuw@knmi.nl), ORCID 0000-0002-1649-6333)

**Abstract:** Air Quality (AQ) is determined by the concentrations of aerosols and trace gases. Aerosol concentration is measured by the mass concentration of particles smaller than 2.5  $\mu\text{m}$  (PM<sub>2.5</sub>) or 10  $\mu\text{m}$  (PM<sub>10</sub>), while trace gases include ozone (O<sub>3</sub>), nitrogen dioxide (NO<sub>2</sub>), sulfur dioxide (SO<sub>2</sub>), and carbon monoxide (CO). Ammonia (NH<sub>3</sub>) and (biogenic) volatile organic compounds ((B)VOCs) also play an important role in atmospheric chemistry affecting the concentrations of trace gases and ultimately AQ. This study focuses on various aspects of AQ in China, utilizing remote sensing data from satellite and ground-based sensors to obtain information on PM emissions and concentrations and AQ-relevant trace gases. This research was conducted within the framework of the ESA/NRSCC MOST collaboration project Dragon 5, as part of the EMPAC (Exploitation of satellite remote sensing to enhance our comprehension of the Mechanisms and Processes influencing Air quality in China) project. It summarizes findings on four main topics: (1) Retrieval of trace gas concentrations and aerosol products from satellite data, validation using ground-based reference data, and interpretation of results in terms of AQ effects, such as the conversion of column-integrated properties to near-surface concentrations; (2) Determination of trace gases emissions relevant to AQ, using satellite data and models; (3) Analysis of time series data on trace gases and aerosols

to assess the impact of emission reduction policies on AQ improvement ; (4) Research contributing to a deeper understanding of mechanisms and processes affecting atmospheric composition about AQ.

Keywords: Earth Observation, Algorithm Development, Validation, Atmosphere, Air Quality, Emissions, Aerosols, Trace Gases, Atmospheric Processes, Trends.

## 1. Introduction

Air quality (AQ) is determined by the concentrations of trace gases and aerosols near the Earth's surface, where they harm Human health (e.g., Brunekreef et al., 2002), ecosystems (e.g., Manisalidis et al, 2020; EPA, 2024a), buildings, cultural heritage and materials (e.g., Varotsos et al., 2009; Rao et al., 2014). Air quality is often indicated by the air quality index (AQI) based on concentrations of trace gases and aerosols (cf. WAQI, 2024; WHO, 2024). In AQ studies, the commonly used proxy for aerosol concentrations is particulate matter (PM), i.e. the integrated mass of particles with in situ diameters smaller than 2.5  $\mu\text{m}$  (PM<sub>2.5</sub>) or 10  $\mu\text{m}$  (PM<sub>10</sub>), from which aerosol water has been removed by weighing them in an environment with low relative humidity (RH). The AQI is calculated as described by, e.g., Yuan et al. (2019) and is determined by the species with the highest concentration (see Fan et al., 2021, for a brief summary). However, the species included may be different between applications. For instance, the trace gases included in the World Air Quality Index (WAQI, 2024) are nitrogen dioxide (NO<sub>2</sub>), sulfur dioxide (SO<sub>2</sub>), ozone (O<sub>3</sub>), carbon monoxide (CO), PM<sub>2.5</sub> and PM<sub>10</sub>, whereas the World's Air Pollution: Real-time Air Quality Index (WAQI, 2024) uses only PM<sub>2.5</sub> and NO<sub>2</sub>. Other trace gases of importance for AQ and effects on Human beings and ecosystems are, for instance, ammonia (NH<sub>3</sub>), formaldehyde (CHCO), and (biogenic) volatile organic compounds ((B)VOCs). The mentioned trace gases are not only important for AQ but also for climate because they act as precursors for aerosols and O<sub>3</sub> which are earmarked as essential climate variables (ECVs) (GCOS, 2024). The concentrations of NO<sub>2</sub>, VOCs, O<sub>3</sub> and aerosols are not independent because of complicated chemical reactions and a reduction of the concentrations of one species may increase another species. This was clearly evidenced during the COVID-19 lockdown periods in China when emissions of NO<sub>2</sub> were strongly reduced but concentrations of O<sub>3</sub> increased substantially (e.g., Huang et al., 2020; Fan et al., 2020a; 2021; Ding et al., 2020; Wang et al., 2021).

The current study focuses on air quality in China. China is a very large country with a wide variety of conditions affecting air quality, with a variety of sources of aerosols and trace gases. China is located in several climate zones, i.e. the alpine climate zone, the temperate continental climate zone, the temperate monsoon climate zone, the subtropical monsoon climate zone, and the tropical monsoon climate zone (Li et al, 2022a). China is influenced by a variety of large-scale weather systems, such as the East Asia Monsoon with warm and wet summer monsoons and cold and dry winter monsoons, the Siberian High, etc., which are responsible for the occurrence of different transport patterns of atmospheric constituents. China also has a wide variety of surface properties, such as deserts, high mountains enclosing large basins, large planes, and oceans to the east and south. In addition, there are various anthropogenic influences with a strong contrast between the densely populated megacities and large industrial and economic centers on one side and the sparsely populated rural areas with agricultural activity and forests on the other. All these different influences render China a large natural laboratory for the study of air quality and climate.

Air quality studies require information on aerosol and trace gas concentrations which usually are provided from ground-based monitoring networks using a suite of instrumentation for the various species (WAQI, 2024). In China, long-term data records, which can be used for air quality studies, are sparse. A national

network of ground-based air quality monitoring stations was established in 2013 and provides concentrations of PM<sub>2.5</sub>, PM<sub>10</sub>, SO<sub>2</sub>, NO<sub>2</sub>, O<sub>3</sub>, and CO. This network is maintained by the China National Environmental Monitoring Center (CNEMC) of the Ministry of Ecology and Environment (MEE, 2024). Hourly and 24-h moving averages for each site or city are used in many air quality studies (Fan et al., 2020a; Xue et al., 2020). However, despite the large number of monitoring sites included in this network, they are concentrated in densely populated regions in cities and industrial areas, which leaves gaps in other areas for which data is not available. The gaps can be filled by using satellite observations with wide spatial coverage. Satellite-based instruments used for trace gas retrieval are spectrometers, while radiometers are used for aerosol monitoring (de Leeuw et al., 2021). Both types of instruments measure the intensity of upwelling solar radiation reflected by the Earth (or Infra-red (IR) radiation emitted by the Earth) from which the required information is retrieved. The instruments used for trace gas retrieval and most sensors used for aerosol retrieval, fly on low Earth orbit (LEO) satellites, which do not provide more than one overpass during daytime, except at high latitudes. This problem can be overcome using several LEO satellites providing several consecutive views per day, or by using geostationary (GEO) satellites which view the Earth's disc every 10 minutes (Earthdata, 2024). GEO satellites usually carry instruments designed for meteorological observations, but some of them are also used for aerosol retrieval, such as the Advanced Himawari Imager (AHI) on board Himawari-8 (H8), developed by the Japan Meteorological Agency (JMA) and launched on October 7, 2014 (JMA, 2024). The Geostationary Environment Monitoring Spectrometer (GEMS), launched by the Republic of Korea in February 2020, is the first satellite instrument to observe air quality (WMO, 2024) as part of a constellation of three satellite instruments (EPA, 2024b), including the ultraviolet and visible spectrometer flying on the Tropospheric Emissions: Monitoring Pollution (TEMPO) mission, launched by the United States National Aeronautics and Space Administration (NASA) on 7 April 2023 (TEMPO, 2024) and by Sentinel-4 on the Meteosat Third Generation Sounder (MTG-S) planned to be launched by the European Organisation for the Exploitation of Meteorological Satellites (EUMETSAT) in 2024 (EUMETSAT, 2024).

Satellite observations provide information on the column-integrated concentrations of trace gases (vertical column densities, VCD) and aerosols (aerosol optical depth, AOD: the column-integrated extinction) inverted from spectrally resolved radiances measured at the top of the atmosphere (TOA). For aerosol retrieval, the use of one or more viewing angles and information on the degree of polarization provide added value allowing not only more accurate retrieval but also for better characterization of the aerosol properties such as aerosol type (Kahn and Gaitley, 2015; Li et al., 2019). The relations between column-integrated and near-surface concentrations of trace gases or between AOD and PM depend on the vertical distribution of the trace gas or aerosol concentrations (as well as optical properties in the case of aerosols) which in turn depend on meteorological factors and chemical reactions (Zhang and Li, 2015; Zhang et al., 2020). When the planetary boundary layer (PBL) is well-mixed, i.e. inert gases are homogeneously distributed from the surface to the top of the PBL, near-surface concentrations can simply be obtained by dividing the column-integrated concentration by the PBL height (PBLH) and, provided that no species occur above the PBL, the satellite retrieved VCD and AOD are representative of the PBL concentration. However, often residual and disconnected layers occur above the PBL with trace gases and aerosols (Liu et al., 2021) which influence the satellite observations but are not related to the near-surface concentrations. Furthermore, the temperature decreases with height above the Earth's surface which may disturb the chemical equilibrium and lead to changes in concentrations due to dissociation in the molecular or solid/liquid phase. An example is the dependence of the equilibrium between ammonium nitrate and ammonia and nitric acid on the ambient temperature (Kang et al., 2022). Another example is the increase of RH with decreasing temperature which results in the swelling of aerosol particles due to condensation of water vapor, which not only changes the particle size but also the aerosol composition and thus the optical properties.

Time series of satellite and ground-based measurements may vary differently in response to changes in meteorological conditions (Fan et al., 2020b) and their seasonal variation may even be opposite, as has been

observed for AOD and PM<sub>2.5</sub> time series (Xu et al., 2019). This may be due to responses to vertical mixing within the PBL and (seasonal) variations of the PBLH, responses to changes in air temperature affecting atmospheric lifetimes and chemical reactions, responses to variations in RH, transport of gases and aerosols due to changes in wind speed (ventilation, turbulent deposition) and wind direction (source regions), cloud processing changing concentrations and chemical composition of aerosol particles, and washout during rain. Large-scale weather systems influence the transport of aerosols and trace gases between source and receptor regions (Hou et al., 2020). Vertical transport mixes the aerosol particles and trace gases throughout the ABL with differences in temperature and RH at different altitudes, and these different meteorological environments affect chemical reactions and the composition of aerosols and concentrations of trace gases as observed in urban heat islands (e.g. Neuman, 2003; Aan De Brugh et al., 2012; Curci et al., 2015; Kang et al., 2022).

The main goal of this study is to gather the key findings derived from the EMPAC project that improve our scientific knowledge of the mechanisms and processes affecting air quality in China. Specifically, we aim to explore how satellite observations can be used more effectively in AQ monitoring. To achieve this aim, the study has outlined the following objectives:

- Develop improved algorithms to invert information on atmospheric composition from satellite observations;
- Improve our understanding of relationships between concentrations of aerosols and trace gases retrieved from satellite observations and those near the surface, through a better understanding of processes affecting these relationships;
- Quantify the emissions of trace gases and aerosol precursors using a top-down approach.

These objectives are achieved by conducting various research studies on different areas, in collaboration between universities and research centers in China and Europe. Satellite sensors along with ground-based remote sensing and in situ measurements (see Section 2 for an overview) are employed to analyze a range of factors influencing air quality in China.

The study is structured along four main topics: (1) retrieval and validation of AOD, PM<sub>2.5</sub>, and NO<sub>2</sub>; (2) emissions of NO<sub>2</sub>, SO<sub>2</sub>, CO<sub>2</sub>, BVOCs, PM<sub>2.5</sub> and PM<sub>10</sub>; (3) time series and trends of AOD and CO; (4) meteorological, physical and chemical processes influencing concentrations of O<sub>3</sub>, NO<sub>x</sub> (NO + NO<sub>2</sub>) and PM<sub>2.5</sub> in the atmosphere. Each of these topics includes findings deduced from several studies performed in the frame of the EMPAC project aimed at enhancing our understanding of air quality processes and evaluating the effectiveness of policies to improve air quality. Section 2 provides an overview of the satellite sensors and other instruments, or techniques, used in this study. An overview of the studies undertaken and the mid-term results is presented in Section 3. Finally, Section 4, briefly discusses the results, summarizes the conclusions, and highlights the accomplishments. A list of abbreviations is provided in the Appendix.

## 2. Materials and Methods

The studies presented in Section 3 are undertaken by different universities and research centers, with the common goal of improving our understanding of different processes in the atmosphere and how these contribute to air pollution. This also requires monitoring of air quality, i.e. monitoring of the concentrations of aerosols (PM<sub>2.5</sub> and PM<sub>10</sub>; sometimes also other mass fractions) and relevant trace gases such as O<sub>3</sub>, NO<sub>2</sub>, SO<sub>2</sub>, CO and other gases affecting these concentrations and / or life on Planet Earth. In particular, this study focuses on the use of a variety of satellites, with different techniques, to obtain information contributing to reaching the objectives. The satellites and sensors are listed in Table 1, together with their application in this study. For validation of the retrieval results, ground-based remote sensing instruments are used which are listed in Table 2 together with instruments used in process studies. The studies were made in different areas which are listed in Table 3.

**Table 1.** Satellites and sensors used in this study.

Sensor	Satellite	launched	characteristics	Application (section)
<b>ESA third party missions</b>				
OMI	Aura	2004	UV/VIS spectrometer	NO <sub>2</sub> data (3.1.5)
	HIMAWARI	2014		
MODIS	TERRA Aqua	1999 2002	Radiometer	AOD time series (3.3.1)
IASI	METOP-A METOP-B METOP-C	2006 2012 2018	Infrared Atmospheric Sounding Interferometer	CO total column concentrations (3.3.2)
OCO-2	LeoStar-2	2014	3 spectrometers in the NIR and MIR	CO <sub>2</sub> data (3.2.3)
<b>ESA, Explorers and Sentinels</b>				
TROPOMI	Sentinel-5p	2017	UV/VIS spectrometer	NO <sub>2</sub> data (3.1.5; 3.1.6; 3.2.1; 3.2.2; 3.2.3)
ALADIN	AEOLUS	2018	Wind profiles	3.4.3
<b>Chinese EO data</b>				
Wide-Field-of-View (WFV) cameras	GF-1 (Gaofen-1)	2013	4 UV/VIS cameras with 16 m spatial resolution	Retrieval of High-Resolution AOD (3.1.4)
Polarized Scanning Atmospheric Corrector (PSAC)	HJ-2 A and B constellations	2020	Polarization, multispectral	AOD retrieval (3.1.1)
Polarization CrossFire (PCF) satellite sensor	GF5-02 DQ-1	2021 2022	Polarization	AOD/PM <sub>2.5</sub> relationship (3.1.2)

**Table 2.** Instruments used for validation and process studies in this study.

Instrument	Purpose	Application (section)
CIMEL CE-318 Sun-photometer	SONET and AERONET networks providing reference data for aerosol retrieval	Validation aerosol retrieval (3.1.3)
AIS antenna and receiver	Collecting AIS signals of ships	(3.1.4)
Multi-AXis Differential Optical Absorption Spectroscopy (MAX-DOAS)	NO <sub>2</sub> profiles	Validation TROPOMI NO <sub>2</sub> retrieval results (3.1.5)
KNMI NO <sub>2</sub> -sonde	Used on quadcopter to measure in situ NO <sub>2</sub> profiles	(3.4.1)
NO <sub>x</sub> analyzer type Thermo Environmental Instruments (TEI) 42	Intercomparison with KNMI NO <sub>2</sub> -sonde	(3.4.1)
ground-based radar wind profiler (RWP) network of China	Validation AEOLUS wind products	(3.4.3)

Tethered balloon	PM2.5 profiles	(3.4.4)
surface-based meteorological and PM2.5 observations, turbulence measurements using a 3-D Sonic Anemometer (CSAT3), and high-resolution soundings	Understanding processes affecting PM2.5	(3.4.4)

**Table 3.** Study regions in this study.

Region	Coordinates	Application in Section
Northeast Asia	30-40 N, 120-140E	3.1.1
Beijing	Radi Site SONET/AERONET 40.005°N, 116.379°E	3.1.3
Xuzhou region (Jiangsu, China)	33.3-35 N, 116.5-118.5 E;	3.1.4, 3.1.5, 3.4.2
Xuzhou, CUMT MAX-DOAS site	34.217 N, 117.142 E	3.1.5, 3.4.2
Arctic	(>70 N)	3.1.6
Yangtze River Delta	26-34 N, 112-124 E.; (Figure 11)	3.2.1, 3.2.2, 3.4.1
Wuhan, Hubei, China	circular region centered at 114° E, 30.7° N, with a diameter of ~ 186 km	3.2.3
Qianyanzhou subtropical coniferous plantation in Taihe county, Jiangxi, China	26°44'48" N, 115°04'13" E	3.2.4
South-Eastern China Below the Hu line (SECBH)	Part of the area between 20-55 N, 100-130 E, encompassing NCP, YRD, PRD, SCB and HNB	3.3.1
Nanjing, Jiangsu, China – Pukou district	32.214 N, 118.658 E	3.4.1
Athens, Greece	38N, 23.7 E	3.4.2
Xiangyang, Hubei, China	32.0090 N, 112.1226 E	3.4.4

### 3. Results

#### 3.1 Retrieval and Observations

In this Section, the development and use of new satellite-retrieved products for aerosols and NO<sub>2</sub> is presented. Aerosol particles are characterized by a number of physical and chemical parameters such as their particle size distribution (the number concentration of particles at each size, where size ranges from a few nm to tens of μm), chemical composition including aerosol water, and particle shape. The particle sizes of importance for satellite remote sensing range from about 0.05 μm to about 10 μm. The chemical composition of the particles determines their hygroscopicity, i.e. the uptake of water vapor by the particles from the atmosphere, as a function of RH and the deliquescence point (the RH at which particles are activated). The uptake or release of water vapor in turn changes the particle size distribution. The chemical composition (including aerosol water) and the size of a particle determine the complex refractive index. Particle size distribution, shape and complex refractive index together determine the interaction of an aerosol with solar radiation, i.e., the scattering and absorption of light by the particles. The light backscattered into space is detected by optical sensors aboard satellites and the scattered signal is used together with a model to retrieve the aerosol properties. This brief summary clearly shows that a suite of

aerosol parameters needs to be measured to accurately determine the aerosol optical and physical properties. A satellite sensor does not provide enough information to do this, and therefore aerosol parameters need to be estimated beforehand (in a forward model) to simulate the signals from the satellite sensor. By comparison of the simulated and measured signals, a limited number of actual aerosol parameters are estimated. Traditionally, satellites only measure the intensity of the scattered radiation at a specific wavelength and viewing angle. By using more wavelengths, several viewing angles and polarization information, the number of degrees of freedom can be increased and aerosols can be better characterized. In this section, the advantage of the use of polarization to improve the AOD retrieval is presented for two Chinese sensors: the Polarized Scanning Atmospheric Corrector (PSAC) (Section 3.3.1) and the Polarization CrossFire (PCF) sensor on board the GF5-02 and DQ-1 satellites (Section 3.3.2). In particular, a new strategy to retrieve PM<sub>2.5</sub> from PCF is presented and uncertainties are discussed. For the validation of aerosol products, the Sun-sky radiometer Observation NETWORK (SONET) is used to provide ground-based reference data (Section 3.1.3) and the use of these data is illustrated for validation of PSAC-retrieved AOD.

To collect enough scattered radiation for aerosol characterization, the sensor needs to be highly sensitive and usually this is achieved at the expense of spatial resolution. In practice, often the signal received over a number of satellite pixels is averaged to achieve a sufficient signal to noise ratio (SNR). However, for monitoring of urban scale air pollution from space, a finer spatial resolution is desirable. A novel method to achieve this is described in Section 3.1.4, where the accurate AOD provided by the most commonly used (for aerosol retrieval) Moderate Resolution Imaging Spectroradiometer (MODIS) is downscaled to a resolution of 100 m by the utilization of data from high-resolution cameras on the Chinese GF-1 satellite.

The TROPOspheric Monitoring Instrument (TROPOMI/Sentinel-5p) provides NO<sub>2</sub> vertical column densities with unprecedented accuracy and spatial resolution. The data over Xuzhou are validated versus ground-based NO<sub>2</sub> VCDs retrieved using a MAX-DOAS (Multi-AXis Differential Optical Absorption Spectroscopy) instrument as described in Section 3.1.5. TROPOMI is the successor of the Ozone Monitoring Instrument (OMI), from which a long NO<sub>2</sub> VCD time series is available since its launch in 2004, but with a larger footprint than for TROPOMI. To extend the TROPOMI NO<sub>2</sub> VCDs to 2004 by using OMI data, the latter are downscaled using a method described in Section 3.1.5. In Section 3.1.6, TROPOMI data are used to determine Lightning NO<sub>2</sub> (LNO<sub>2</sub>) productivity over the Arctic and the results are compared with the productivity from other NO<sub>2</sub> emission sources in the Arctic.

### *3.1.1 Improving aerosol remote sensing using polarization measurements*

The PSAC was launched on board the HJ-2 A and B constellations on September 27, 2020. PSAC provides advanced measurements of aerosols, clouds and water vapor, with a focus on atmospheric correction for the charge-coupled device (CCD) camera, the hyperspectral imager (HIS) and the infrared spectroradiometer (IRS) onboard the same satellite platforms.

Examples of PSAC false color maps and corresponding AOD retrieval results over land are presented in Figure 1. In general, thanks to the additional simultaneous polarization measurements, the AOD retrieval results show good performance compared with traditional AOD remote sensing based on intensity-only satellite sensors such as MODIS.

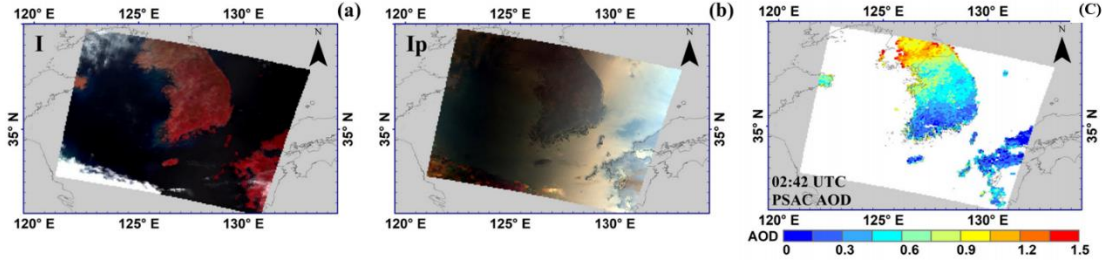


**Figure 1.** PSAC observations and retrieved AOD over Northeast Asia on April 11, 2021. (a) PSAC false-color map synthesized using nonpolarized data. (b) PSAC false-color map synthesized using polarization data. (c) Corresponding AOD retrieval results. (Figure adapted from Li et al., 2022b).

### 3.1.2 New polarimetric satellite sensor suits applied to derive the AOD/PM<sub>2.5</sub> relationship

Studies of the AOD/PM<sub>2.5</sub> relationship benefit from the new generation of optical and microphysical aerosol parameters obtained from advanced polarimetric satellites. China has launched the GF5-02 and DQ-1 satellites, on 7 Sep, 2021 and 16 Apr, 2022, respectively, carrying the most advanced Polarization CrossFire (PCF) satellite sensors. The corresponding retrieval strategy, using the Particulate Matter Remote Sensing (PMRS) model (Zhang and Li, 2015; Zhang et al., 2020), was then applied to PCF data for the retrieval of PM<sub>2.5</sub> from space.

In the PMRS model, PM<sub>2.5</sub> mass concentrations near the ground are calculated from five aerosol physical and optical parameters, i.e. AOD, fine mode fraction (FMF), aerosol layer height (ALH), fine-mode columnar volume-to-extinction ratio ( $VE_f$ ), effective density of fine-mode aerosol particles ( $\rho_f$ ), and the volume hygroscopic growth function ( $f(RH)$ ), which represents the ratio of the total volume of particulate matter to the dry volume, based on the RH of the surrounding air. The approaches to estimate PM<sub>2.5</sub> using these parameters are described in detail in Zhang and Li (2015) and Zhang et al. (2020).

The PMRS model inevitably has some uncertainties. The sensitivity to assumptions in the calculation of PM<sub>2.5</sub> from AOD observations using the PMRS model are presented in Figure 2, together with the corresponding statistical metrics for comparison of the retrieval results with the input data. In Figure 2, the x-axis represents the assumed truth (input) values, and the y-axis represents the corresponding retrieval results. The impact of using the fine mode AOD, obtained by multiplying AOD by FMF, to calculate the extinction contribution to PM<sub>2.5</sub>, is presented in Figure 2(a). Figure 2(a) shows the good correlation (with  $R^2$  of 0.99) between the input and output values of  $AOD \times FMF$ . Hence, the uncertainties caused by the size cutting procedure are small.

As regards the volume visualization procedure, the AOD is converted to volume concentration through  $VE_f$  which is calculated from the FMF (Li et al., 2017). The relatively large uncertainty in the retrieved FMF, especially for small FMF values, is transferred directly to  $VE_f$ , resulting in the offset of some data pairs from the identity line in Figure 2(b).

The mass density weighting procedure in Figure 2(d) was realized using the semi-empirical relationship between  $\rho_f$  and the real part of complex refractive index of dry fine mode particles  $m_r^f$ . Due to the small variation of  $VE_f$  and  $\rho_f$ , the uncertainties introduced by the volume visualization procedure, and the weighting procedure, both are relatively small.

The bottom isolation procedure is conducted by using PCF retrievals of aerosol layer height. By using ALH, the ratio of the extinction coefficient near the ground to the total aerosol optical depth can be obtained. The line fitted to the data points in the scatter plot in Figure 2(c) has a slope close to 1 and a small offset. Compared with the other procedures, there is a higher cost performance to effectively improve the accuracy of aerosol layer height retrieval.

To account for the difference in AOD and PM<sub>2.5</sub> due to the measurement of AOD in ambient RH conditions, versus measurements of PM<sub>2.5</sub> at low RH conditions, i.e. dry aerosol mass, the hygroscopic growth factor  $f(\text{RH})$  was used. To achieve this,  $f(\text{RH})$  was estimated using assumptions on the real part of the refractive index for wet and dry particles (Zhang et al., 2017). The results are presented in Figure 2(e). The uncertainties in  $f(\text{RH})$  may come from retrieval errors of the input  $m_r^f$ , or the assumed value of the dry particulate matter. The aerosol hygroscopic properties of aerosol particles are related to their chemical composition. For the same ambient humidity, the hygroscopic growth factors of different aerosol types are obviously different and may range from 1.0 to 3.0. For particles with the same chemical composition, the hygroscopic growth factor increases with the increase of ambient humidity. Direct humidity correction from satellite data depends on the development of sensors and the improvement of inversion techniques in the future. Using the PMSR model, PM<sub>2.5</sub> can be retrieved from PCF synthetic data as shown in Figure 2f.

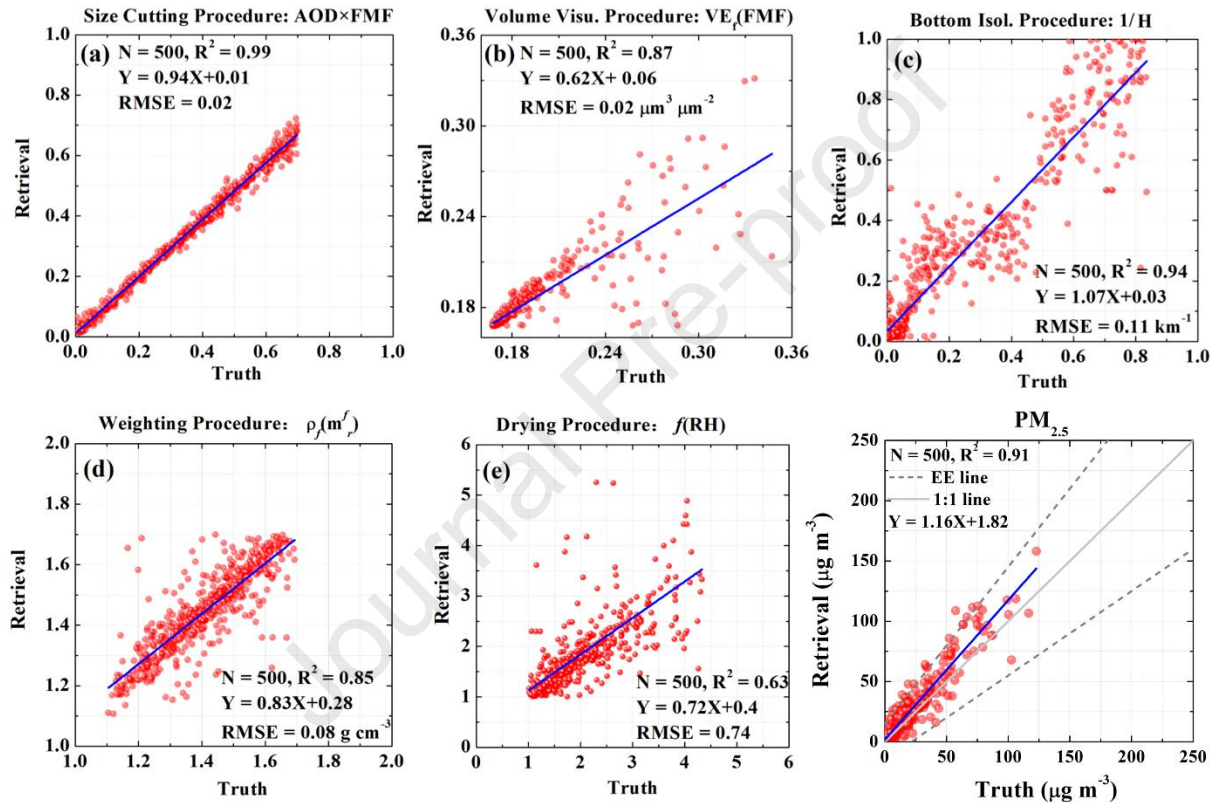


**Figure 2.** Propagation of errors due to assumptions in the PMRS model: (a) size cutting procedure, (b) volume visualization procedure, (c) bottom isolation procedure, (d) mass density weighting procedure, (e) hygroscopic growth factor drying procedure, and (f) scatterplot of the retrieved PM<sub>2.5</sub> versus synthetic data, with an expected error (EE) of  $\pm(30\%PM_{2.5} + 15) \mu\text{g m}^{-3}$ . (Figure adapted from Li et al., 2022c).

### 3.1.3 Validation of PSAC-retrieved AOD using SONET sun photometer reference data

To assess the aerosol remote sensing performance of the PSAC sensors onboard the HJ-2 A/B satellites, time series of satellite AOD in China are compared with ground-based reference measurements from the SONET network (for a map of the SONET location and a description of the SONET network, see Li et al., 2018). SONET complements NASA's Aerosol Robotic Network (AERONET) sun photometer network (Holben et al, 1998; AERONET, 2024), with some sites in China in common. SONET follows the same procedures as AERONET. As an example for the use of SONET data, time series of AOD ground-based measurements from the CIMEL CE-318 Sun-photometer at the Beijing\_RADI site (40.005°N, 116.379°E)

and PSAC-retrieved AOD are compared as shown in Figure 3a. The time series in Figure 3a show the good comparison between the two data sets.

For validation, the mean value of the SONET AOD observations within half an hour of the satellite overpass time is matched with the spatial average of satellite-retrieved AOD within an area of 50 km x 50 km centered on the SONET site. A valid match between SONET data and remote sensing data must meet two requirements at the same time: i) the number of valid satellite retrievals within the area of 50 km x 50 km centered on the SONET site is not less than five and ii) the number of SONET observations within half an hour of the satellite observation time is not less than two. A scatter plot of the collocated PSAC-retrieved AOD and the AERONET/SONET AOD observations is presented in Figure 3b. This comparison shows that 68.6% of the data are within the expected error (EE) of  $\pm(0.05 + 0.2 * AOD_{SONET})$  (PER20) required for in-orbit test objectives.

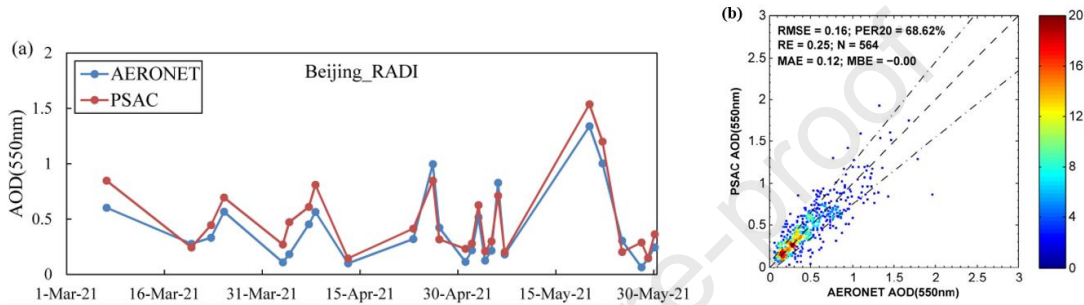


**Figure 3.** (a) Time series comparison of AOD obtained from SONET measurements and retrieved from PSAC data at the Beijing\_RADI site. (b) Scatter density plot of collocated PSAC and AERONET data during the period from March 2021 to May 2021. The dotted line in the middle is the 1-1 line. The dotted lines on either side of the identity line are the envelope of PER20. (Figure adapted from Li et al., 2022b).

### 3.1.4 Retrieval of High-Resolution Aerosol Optical Depth for Urban Air Pollution Monitoring

Aerosol Optical Depth (AOD) is a key physical quantity to characterize atmospheric turbidity and air pollution. Accurate retrieval of AOD is of great importance for air quality assessment. The satellite sensors which are currently used for AOD retrieval (Sogacheva et al., 2020) provide AOD with a spatial resolution of 1 km (Lyapustin et al., 2018) or more. For AQ applications on local to regional scales, AOD information on spatial scales smaller than 1 km would be desirable. However, the provision of observations at scales of 10s of meters usually suffers from a long revisit time (Sun et al., 2017). As a compromise, the Chinese Gaofen-1 (GF-1) satellite, with four Wide-Field-of-View (WFOV) cameras which together cover a wavelength range from 0.45  $\mu\text{m}$  to 0.89  $\mu\text{m}$  with a spatial resolution of 16 m, is proposed to be used. The four cameras have a combined overlapping swath of 830 km and the revisit time is 4 days. Gaofen-1 was launched in April 2013 into a sun-synchronous orbit at an altitude of 645 km and an inclination of 98°, with a revisit frequency maximum of 4 days. It is the first spacecraft in the civilian China High-Resolution Earth Observation System (CHEOS). For more detail, see eoPortal (2024).

GF-1 data were used together with MODIS Terra and Aqua data to obtain AOD with a spatial resolution of 100 m. To this end, the Synergetic Retrieval of Aerosol Properties (SRAP) algorithm (Xue et al., 2014) was applied to the two MODIS data sets in synergy to obtain AOD with 1 km resolution and the GF-1 wide-field-of-view data were used to further downscale the 1 km MODIS data based on the mutual information method (Li et al., 2012). This method was developed for application over Beijing (Bai et al., 2022) and in the current project it is applied to data over the Xuzhou region (Jiangsu, China; 33.3-35 N, 116.5-118.5 E). As an example, the AOD spatial distribution over this region on May 18, 2020, is presented in Figure 4, showing the detailed information on the AOD resulting from the high spatial resolution (100 m). The AOD spatial distribution provides information on the occurrence of aerosol air pollution across the study area,

which is affected by the direct emission of aerosol particles, the emission and concentration of aerosol precursor gases and meteorological conditions. Preliminary validation of the retrieval results has been carried out by comparison with AERONET ground-based observations. The results are presented in Figure 5 and the statistical analysis shows that the correlation coefficient is 0.85, the root-mean-square error is 0.14 and 51% of the data are within the expected error envelope (EE) of  $\pm 0.05 \pm 0.2 \tau_a$ , where  $\tau_a$  is the AERONET AOD. The experimental results show that the method has high precision, and further verification work is continuing.

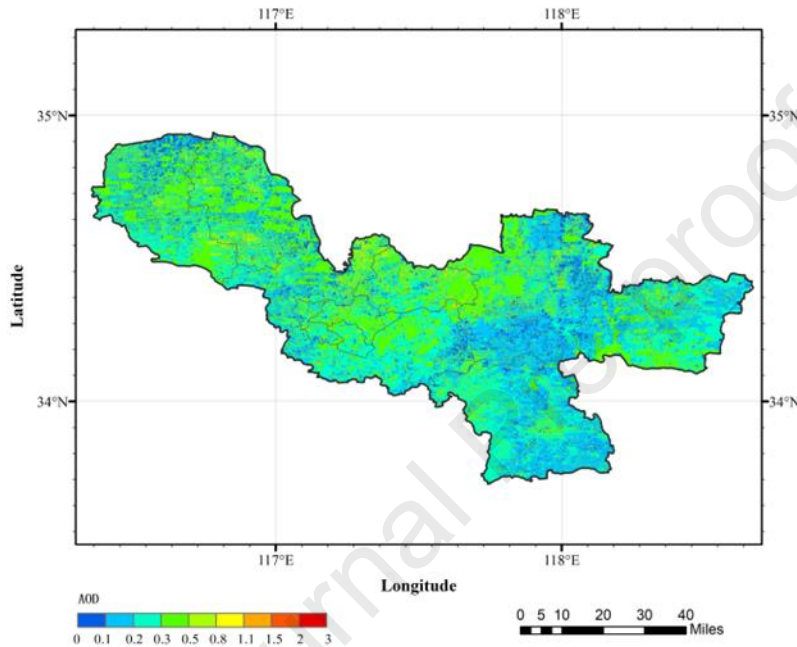


**Figure 4.** Spatial distribution of retrieved AOD, with a spatial resolution of 100 m, over the Xuzhou area on May 18, 2020.

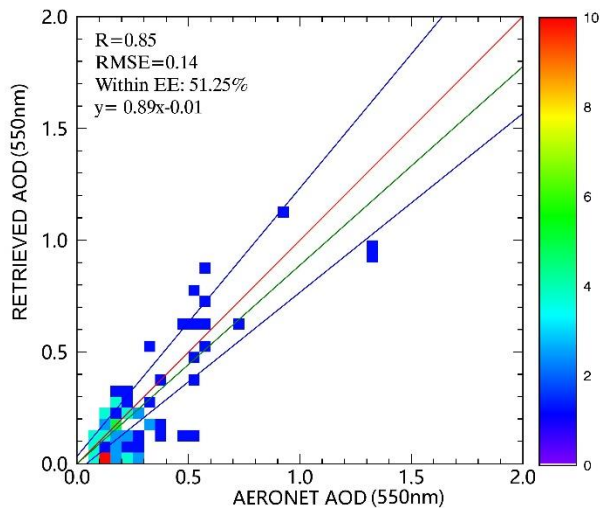


**Figure 5.** Scatter density plot of retrieved 100m AOD versus AERONET data in Xuzhou (Jiangsu, China). Statistical metrics are presented in the top left corner. The red line is the 1:1 line, the green line is the LSQ fit line given in the legend, and the blue lines indicate the expected error envelope ( $EE = \pm 0.05 \pm 0.2 \tau_a$ ), where  $\tau_a$  is the AERONET AOD.

### 3.1.5 Validation of TROPOMI NO<sub>2</sub> and exploring the utility of high-resolution NO<sub>2</sub> columns from TROPOMI

Satellite remote sensing techniques can provide detailed information on the spatial and temporal distribution of NO<sub>2</sub> in the troposphere, which enables us to monitor changes in NO<sub>2</sub> levels over time and assess the effectiveness of emission reduction measures. TROPOMI/Sentinel-5p is particularly useful for identifying pollution sources within individual urban areas, as it has a higher spatial resolution than other sensors (3.5×7.0 km<sup>2</sup> before August 6, 2019, and 3.5×5.5 km<sup>2</sup> at nadir thereafter), with daily global coverage. To evaluate the performance of the TROPOMI NO<sub>2</sub> data for this application, the S5P-PAL reprocessing were compared with offline products (processor versions are earlier than v2.3.1) and with ground-based Multi-AXis Differential Optical Absorption Spectroscopy (MAX-DOAS) observations in Xuzhou (a city in the Jiangsu province in eastern China, see Section 3.1.4).

The TROPOMI data shows a strong correlation with MAX-DOAS measurements, with monthly correlation coefficients (R) reaching as high as 0.92 under quality assurance (QA) thresholds above 75%. However, a tendency to underestimate NO<sub>2</sub> levels is observed, particularly during high pollution episodes (Figure 6a). When comparing the PAL\_v2.3.1 dataset with earlier offline versions, PAL data was found to be consistently higher by 17-48% from December 2019 to November 2020, with seasonal variability (Figure 6b).

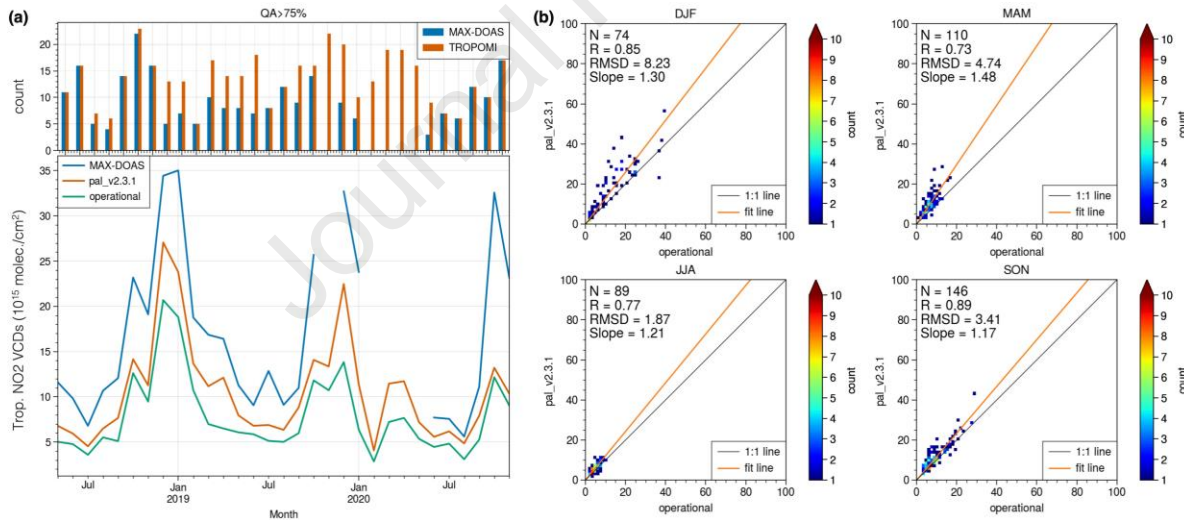


**Figure 6.** Comparison of TROPOMI and MAX-DOAS NO<sub>2</sub> data under QA > 75%. (a) Monthly time series of tropospheric NO<sub>2</sub> comparisons between TROPOMI and MAX-DOAS instruments over the study region from 2018 to 2020. (b) Scatter plots comparing TROPOMI's updated PAL\_v2.3.1 data product with the earlier offline version from December 2019 to November 2020.

Spatial representativeness varies across the scanline, with reduced precision in edge pixels due to high viewing zenith angles (VZA), which introduces greater difference (Figure 7). The results show that the size of the footprint can affect the validation results, and the smaller pixels (<29 km<sup>2</sup>, 2°<VZA<34°) have a higher correlation with MAX-DOAS (R=0.91) when compared to larger pixels (>53.55 km<sup>2</sup>, 47°<VZA<65°).

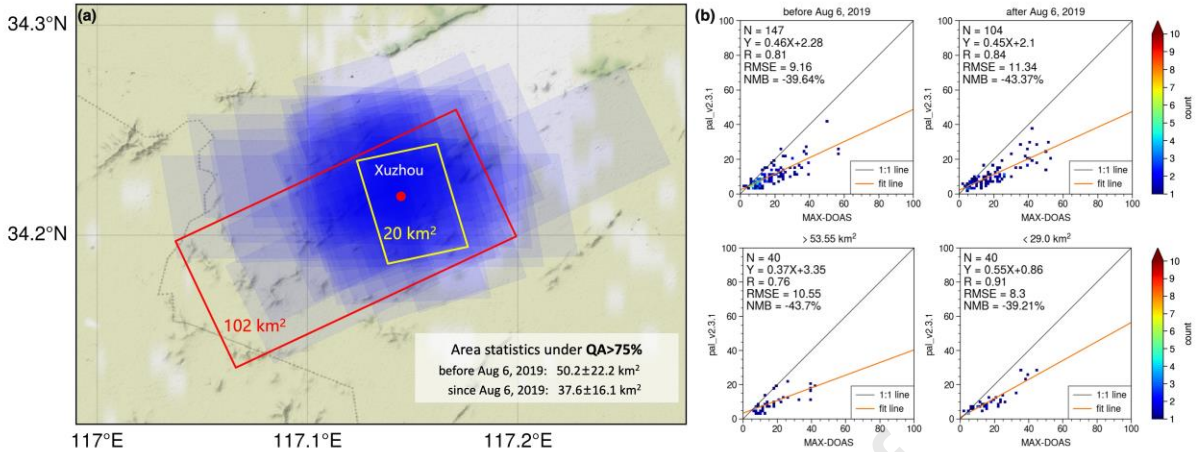


**Figure 7.** Influence of spatial resolution and viewing zenith angle (VZA) on TROPOMI's NO<sub>2</sub> validation. (a) Map showing the spatial coverage area used for TROPOMI and MAX-DOAS comparison around Xuzhou, highlighting the areas with varying pixel footprints. (b) Comparison of TROPOMI and MAX-DOAS NO<sub>2</sub> for pixels with different footprints. In addition, a downscaling framework was proposed to generate high-resolution (0.05°) NO<sub>2</sub> columns from OMI/Aura retrievals. OMI has provided continuous measurements since 2004 but with relatively low spatial resolution (13×24 km<sup>2</sup> at nadir). We compared the performance of two machine learning models: extreme gradient boosting (XGBoost, Figure 8a), and super-resolution convolutional neural network (SRCNN, Figure 8b). The XGBoost method (Chen & Guestrin, 2016) uses pixels from the common observation period of TROPOMI and OMI after 2018 to derive the relationship between high- and low-resolution NO<sub>2</sub> concentrations and was applied to the historical OMI dataset for capturing finer spatial variability and pollution gradients in urban environments, enhancing air quality assessments in densely populated areas. The SRCNN model (Dong et al., 2014) extracts features using 64 convolutional layers with a 9×9 kernel, then applies 32 layers with a 1×1 kernel to map the high-dimensional tensor representation to another set, corresponding to the high-resolution image features. Finally, a single 5×5 convolutional layer reconstructs the high-resolution image.

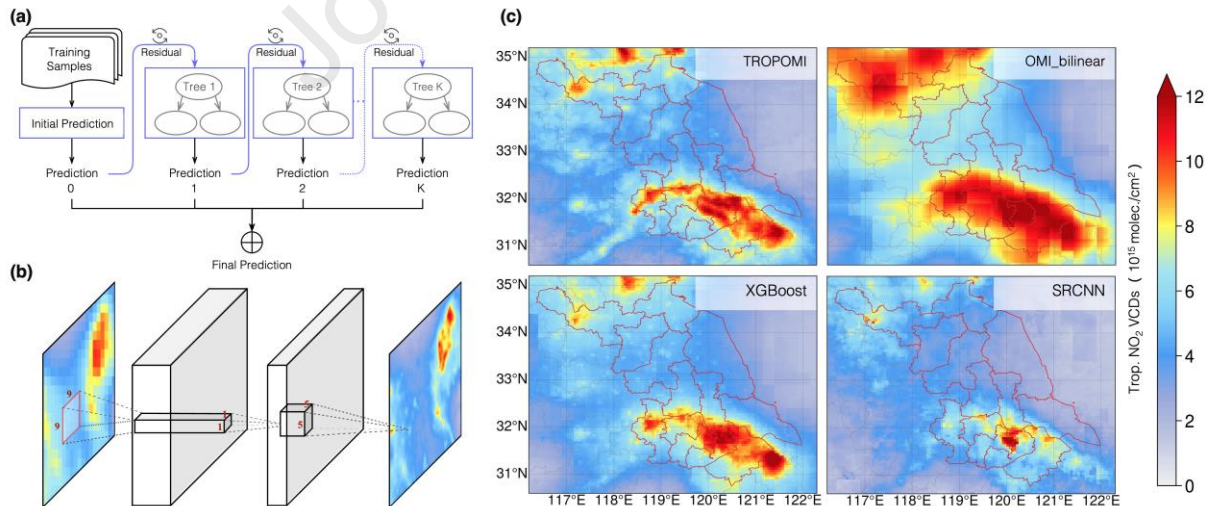


**Figure 8.** NO<sub>2</sub> downscaling framework using machine learning. (a) XGBoost model structure. (b) SRCNN architecture for enhancing spatial resolution. (c) Comparison of NO<sub>2</sub> maps generated by TROPOMI, OMI bilinear interpolation, XGBoost, and SRCNN.

When compared to direct bilinear interpolation of OMI (Figure 8c), XGBoost predictions outperforms with a 10.55 dB increase in Peak Signal-to-Noise Ratio (PSNR) and a 0.09 improvement in Structural Similarity Index (SSIM). SRCNN also improves over bilinear interpolation, though with more modest gains in PSNR (2.61 dB) and SSIM (0.06).

Its serendipitous capability was then explored with the advantages of the orbital characteristics and the high spatial resolution of the sensor. It shows that at latitudes higher than  $35^\circ$ , the Sentinel-5p orbits allow for two observations within an interval of 100 minutes with a probability greater than 20%. By utilizing these overlapping TROPOMI orbits at high latitudes, a model-free inversion approach (Qin et al., 2023; Li et al., 2023; Liu et al., 2024) was applied, based on a dynamic balance among  $\text{NO}_x$  emissions, chemical decay, and advective transport (Figure 9). This approach enables quantification of diurnal  $\text{NO}_x$  emissions from observed tropospheric  $\text{NO}_2$  column values while flexibly incorporating various atmospheric processes and conditions. Overall, the utility of overlapping  $\text{NO}_2$  columns for investigating diurnal variability was demonstrated and the importance of the spatial scale when analyzing and interpreting  $\text{NO}_2$  data was highlighted.

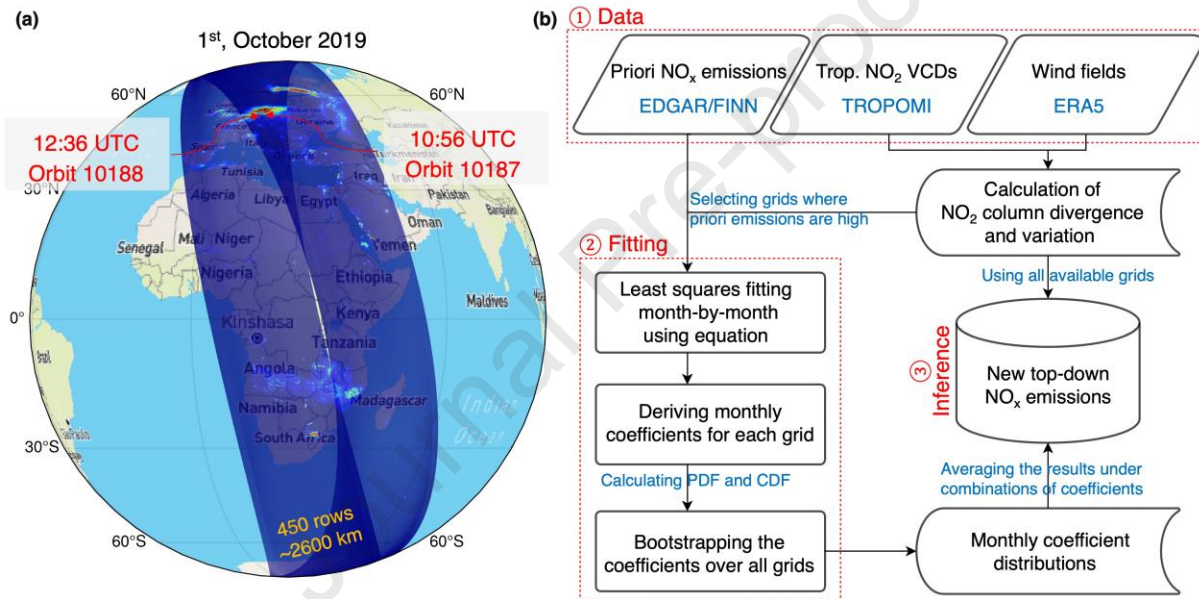


**Figure 9.** Model-free inversion of diurnal  $\text{NO}_x$  emissions using overlapping TROPOMI orbits. (a) Illustration of overlapping orbits enabling two observations within 100 minutes. (b) Schematic of the model-free inversion framework.

### 3.1.6 Spaceborne observations of lightning $\text{NO}_2$ in the Arctic

Lightning is the dominant source of upper tropospheric nitrogen oxides, which are precursors for ozone and hydroxyl radicals. The Arctic region is experiencing notable warming as well as increasing lightning. To evaluate lightning  $\text{NO}_2$  ( $\text{LNO}_2$ ) production in the Arctic, TROPOMI  $\text{NO}_2$  observations during the summer months (June–August) in 2019–2021 have been combined with the Vaisala Global Lightning Dataset 360 (GLD360). Figure 10a shows the mean tropospheric  $\text{NO}_2$  column density over the Arctic region, together with the locations of anthropogenic  $\text{NO}_2$  sources. Consecutive TROPOMI  $\text{NO}_2$  observations have been used to determine the production efficiency and lifetime of  $\text{LNO}_2$  in the Arctic during the 2019–2021 summer months. Our results show that the  $\text{LNO}_2$  production efficiency over the ocean is about 6 times higher than that over continental regions. Moreover, the 3 hours lifetime of  $\text{NO}_2$  in the Arctic is similar to that in mid-latitude polluted regions. Additionally, we find that higher  $\text{LNO}_2$  production efficiency often correlates with lower lightning rates. The summertime lightning  $\text{NO}_x$  emission in the Arctic (north of  $70^\circ$

N) is estimated to be  $219 \pm 116 \text{ Mg(N)}$ , which is equal to 5% of the anthropogenic  $\text{NO}_x$  emissions. However, as illustrated in Figure 10b, for the span of a few hours, the Arctic  $\text{LNO}_2$  density can be comparable to the anthropogenic  $\text{NO}_2$  emissions in the region. Assuming a  $\text{NO}_x$  to  $\text{NO}_2$  ratio of 2.4, we compare the  $\text{LNO}_x$  emission ( $73 \text{ Mg(N) month}^{-1}$ ) with anthropogenic and soil  $\text{NO}_x$  emissions during the summer. Soil emissions, totaling  $2670 \text{ Mg(N) month}^{-1}$ , dominate  $\text{NO}_x$  over the Arctic land, while anthropogenic  $\text{NO}_x$  emissions of  $350 \text{ Mg(N) month}^{-1}$  over land are roughly the same in magnitude as the wildfire emission of  $430 \text{ Mg(N) month}^{-1}$ . Ship emissions, totaling  $1160 \text{ Mg(N) month}^{-1}$ , are the primary source of  $\text{NO}_x$  over the Arctic ocean. However, the  $\text{LNO}_x$  contributes 93% of  $\text{NO}_x$  in the northeastern region of the Arctic ( $90^\circ$ – $180^\circ \text{ E}$ ,  $80^\circ$ – $90^\circ \text{ N}$ ). These new findings suggest that  $\text{LNO}_2$  can play an important role in chemical processes in the upper troposphere/lower stratosphere in the Arctic region, particularly during the summer. For additional information, see Zhang et al. (2023a).

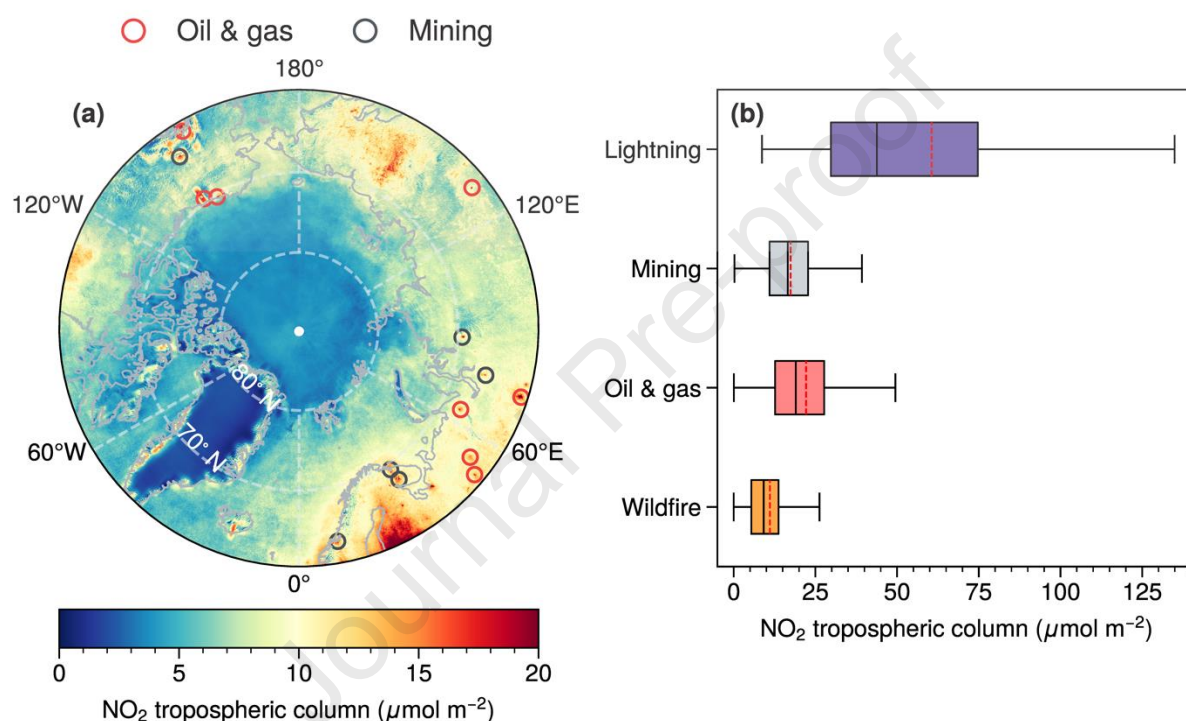


**Figure 10.** (a) Mean  $4 \text{ km} \times 4 \text{ km}$  TROPOMI tropospheric  $\text{NO}_2$  column density in the local afternoon during June–August of 2019–2021. Mining and oil & gas stations are indicated by gray and red circles, respectively. (b) Comparisons of  $\text{NO}_2$  column densities resulting from four sources: lightning, mining, oil & gas, and wildfire. The bar for lightning represents the maximum  $\text{NO}_2$  values over pixels for each lightning case. The wildfire, mining, and oil & gas bars are the daily maximum  $\text{NO}_2$  values at typical locations. The lines inside the box are the median (black) and mean (red) values, respectively. The lower and upper box boundaries are the 25th and 75th percentiles, respectively. The lower and upper error lines are 10th and 90th percentiles, respectively.

### 3.2 Emissions

Satellite data can be used to retrieve column-integrated concentrations of trace gases and aerosol which in turn can be used to derive emissions by inverse modeling. This is illustrated in Section 3.2.1 where TROPOMI-retrieved  $\text{NO}_2$  VCDs are used with the Daily Emissions Constrained by Satellite Observations (DECISO) algorithm to determine high-resolution  $\text{NO}_x$  emissions over the Yangtze River Delta (YRD) region. In Section 3.2.2, a methodology is described for the use of these data to identify emissions from

ships on the Yangtze River in the region of Nanjing. An alternative method for the determination of NO<sub>x</sub> emissions based on TROPOMI observations and CO<sub>2</sub>:NO<sub>x</sub> emission ratios, applied to determine emissions from the city Wuhan, is described in Section 3.2.3. Results from the analysis of BVOC emission fluxes measured over a coniferous plantation, as a function of driving parameters, are presented in Section 3.2.4.

### 3.2.1 High-resolution NO<sub>x</sub> emissions for the YRD region

To derive NO<sub>x</sub> emissions, the latest version of the DECSO inversion algorithm, version 6.1, has been used. DECSO has been applied to NO<sub>2</sub> observations of the TROPOMI instrument on the Sentinel 5p satellite. The NO<sub>2</sub> data has recently been reprocessed with the retrieval algorithm v.2.3.1, known as the PAL data collection (TEMIS, 2024).

The NO<sub>x</sub> emissions are derived at a resolution of 0.1° x 0.1° (about 10 km x 10 km) over the region of the Yangtze River Delta which includes the megacities Wuhan, Hefei, Nanjing, Hangzhou, and Shanghai. The results for 2019 are presented in Figure 11 and clearly show the high emissions along the Yangtze River as well as from large urban centers with high emissions from industry, transportation, and households. In particular, the large emissions in the eastern part of the study area, encompassing Shanghai, Hangzhou and Ningbo are evident, and further upstream of the Yangtze, Nanjing and Wuhan are large sources of NO<sub>2</sub>. High emissions are also observed in the valleys extending to the southwest of Hangzhou and to the west of Ningbo to Jinhua, Shangrao, Nanchang and Changsha and from Changsha to Wuhan. The emission data along the Yangtze River are used in the study on the importance of NO<sub>x</sub> emissions from inland ships on the Yangtze River (Section 3.2.2).

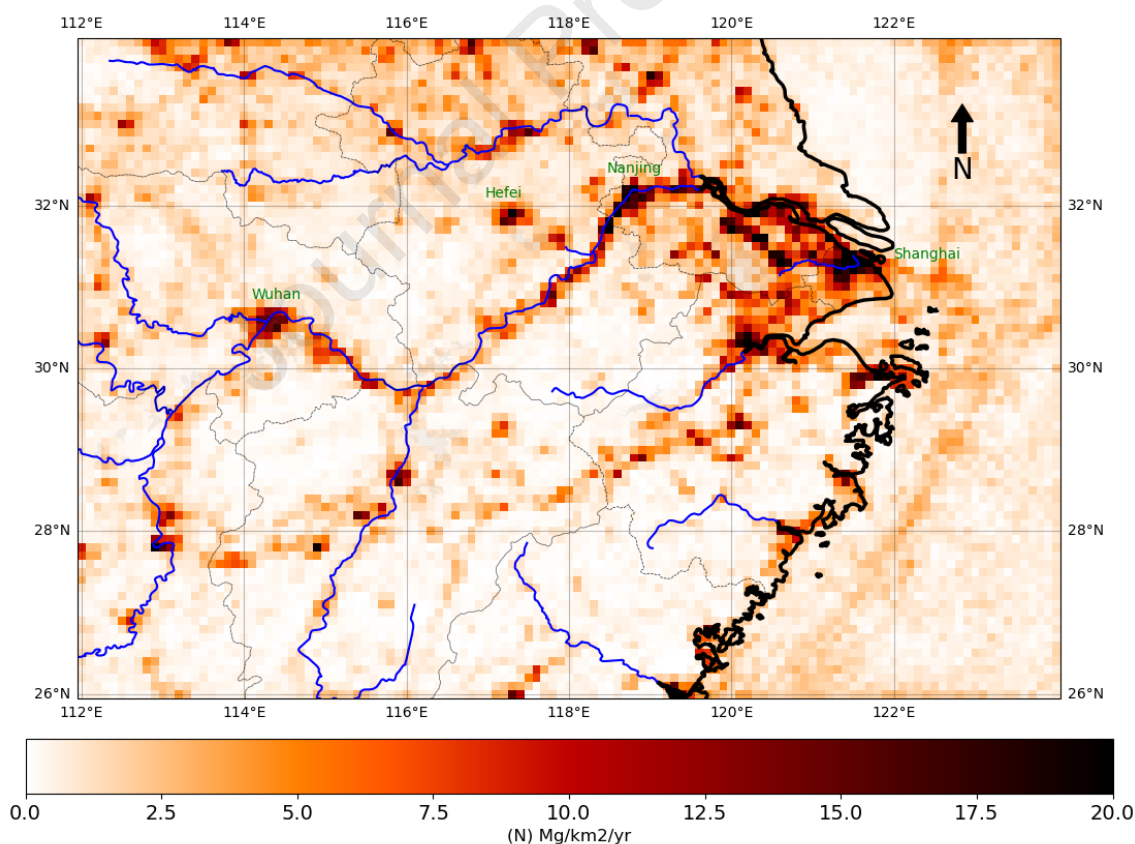


**Figure 11.** Annual mean NO<sub>x</sub> emissions for 2019 from the Yangtze River Delta region (26-34 N, 112-124 E., resolution 0.1°x0.1°) derived from Sentinel 5p (TROPOMI) observations using the DECSO inversion algorithm.

### 3.2.2. *The impact of inland ship emissions on air quality*

With the rapid economic growth, China's ports and shipping industry has achieved unprecedented development, while aggravating air pollution. As shown in Figure 11, emissions along the Yangtze River are very high, which may be due to both intensive industrial and associated other anthropogenic activities along the river, together with the large number of domestic inland river vessels. However, information on the contributions of these sources is very limited due to limited legislation for emission control and the absence of monitoring infrastructure. In order to explore how the information on inland river vessel emissions can be improved, a ship emission inventory has been compiled for the Yangtze River in the region of Nanjing, based on real-time information received from Automatic Identification System (AIS) signals and the China Classification Society (CCS) database. A method has been developed to use AIS signals to calculate ship emissions per vessel. The total ship emissions for NO<sub>x</sub>, SO<sub>2</sub>, PM10 and PM2.5 in the observation area have been estimated for the period from September 2018 to August 2019, showing that the ship emissions were highest during the summer. Cargo ships dominate in the Jiangsu section of the Yangtze River with 81% of the total number of ships and contribute the highest NO<sub>x</sub> emissions, 64.4%, to the total ship emissions. The calculated inland ship NO<sub>x</sub> emissions have been compared with the total NO<sub>x</sub> emissions in the same region derived from TROPOMI observations using DECSO (Section 3.2.1), the Multi-resolution Emission Inventory for China (MEIC, 2024; Li et al., 2017; Zheng et al., 2018a and the Shipping Emission Inventory Model (SEIM)(MEIC, 2024) . The spatial distribution of NO<sub>x</sub> from the ship emission inventory is consistent with that from other inventories, with riverine cities having higher NO<sub>x</sub> pollution than non-riverine cities. Emissions of NO<sub>x</sub> and SO<sub>2</sub> from inland vessels have a significant impact on air pollution along the river, each accounting for at least 40 %. For additional information, see Zhang et al. (2023b).

### 3.2.3 *Top-Down emission estimates NO<sub>x</sub> and CO<sub>2</sub>*

The day-to-day quantification and control of emissions of nitrogen oxides (NO<sub>x</sub>) and CO<sub>2</sub> from a large urban source is addressed using an improved top-down method. Daily observations from the TROPOMI sensor and CO<sub>2</sub>:NO<sub>x</sub> emission ratios from two state-of-science emission inventories are used to estimate day-to-day NO<sub>x</sub> and CO<sub>2</sub> emissions from the Chinese city Wuhan. The model used is inspired by the work of Lorente et al. (2019), who developed a superposition column model to constrain daily NO<sub>x</sub> emissions and applied it to Paris. In the current study, the superposition model was improved by accounting for changes in the background NO<sub>2</sub> density in the study domain along the wind direction, which made it suitable to monitor NO<sub>x</sub> emissions from cities like Wuhan, located in a polluted background. Using the improved top-down method, urban NO<sub>x</sub> and CO<sub>2</sub> emissions were obtained for 50 individual days between September 2019 and August 2020, including several days during the COVID-19 lockdown period. The top-down emissions closely capture the day-by-day variation of NO<sub>x</sub> and CO<sub>2</sub> emissions from Wuhan, revealing only a weak 'weekend effect' and a stronger 'holiday effect' compared to bottom-up emission inventories. Also, the abrupt decrease and slow rebound of NO<sub>x</sub> and CO<sub>2</sub> emissions due to the lockdown in early 2020 were caught. CO<sub>2</sub> emissions were verified for two days with OCO-2 observations close to Wuhan, showing good agreement between predicted and observed CO<sub>2</sub> column mixing ratios, despite considerable differences in emission strength and wind speed between these two days. This work demonstrates that the improved superposition model, driven by satellite NO<sub>2</sub> measurements and verified by satellite CO<sub>2</sub> measurements, is a promising new tool for quantification of city NO<sub>x</sub> and CO<sub>2</sub> emissions, allowing policy makers to gain rapid insights into spatio temporal emission patterns and the effectiveness of carbon and nitrogen regulation in urban environments. For additional information, see Zhang et al. (2023c).

### 3.2.4 Emission fluxes of isoprene and monoterpenes and their affecting factors

Emission fluxes of isoprene and monoterpenes (in this study referred to as BVOCs) in the Qianyanzhou subtropical coniferous plantation in Taihe County, Jiangxi Province, China (26°44'48" N, 115°04'13"), were calculated for the period from May 2013 to December 2016, using an empirical model for BVOC emissions (EMBE) (Bai and Duhl, 2021). EMBE is formulated in terms of the following parameters: S/Q (S and Q are diffuse and global solar radiation), PAR (photosynthetically active radiation), air temperature T, relative humidity RH and water vapor pressure  $p_E$ . To investigate the sensitivity of BVOC fluxes to each of these parameters, the calculated BVOC fluxes were binned into intervals according to S/Q with an S/Q bin width of 0.05, for S/Q ranging from 0 to 1. A plot of the fluxes of isoprene, monoterpene and the sum of these two species versus S/Q is presented in Figure 12a. The data show low emissions at low S/Q, and increase with increasing S/Q. However, when S/Q exceeds a certain value, the emissions decrease. Because of the large scatter in the individual data, it is hard to determine the turning point, i.e. the S/Q value for which the emissions start to decrease. Therefore, curves were fitted to the data for each species, as shown in Figure 12a, and the S/Q value of the turning point was determined as the maximum in this smoothed curve, i.e. at S/Q=0.55. Following a similar procedure, the turning point for air temperature has been determined at T=26 °C and for water vapor pressure at  $p_E=24$  hPa. The data in Figure 12d show that the BVOC emission fluxes increase linearly over the whole range of PAR values observed during the measurements in the Qianyanzhou subtropical coniferous plantation.

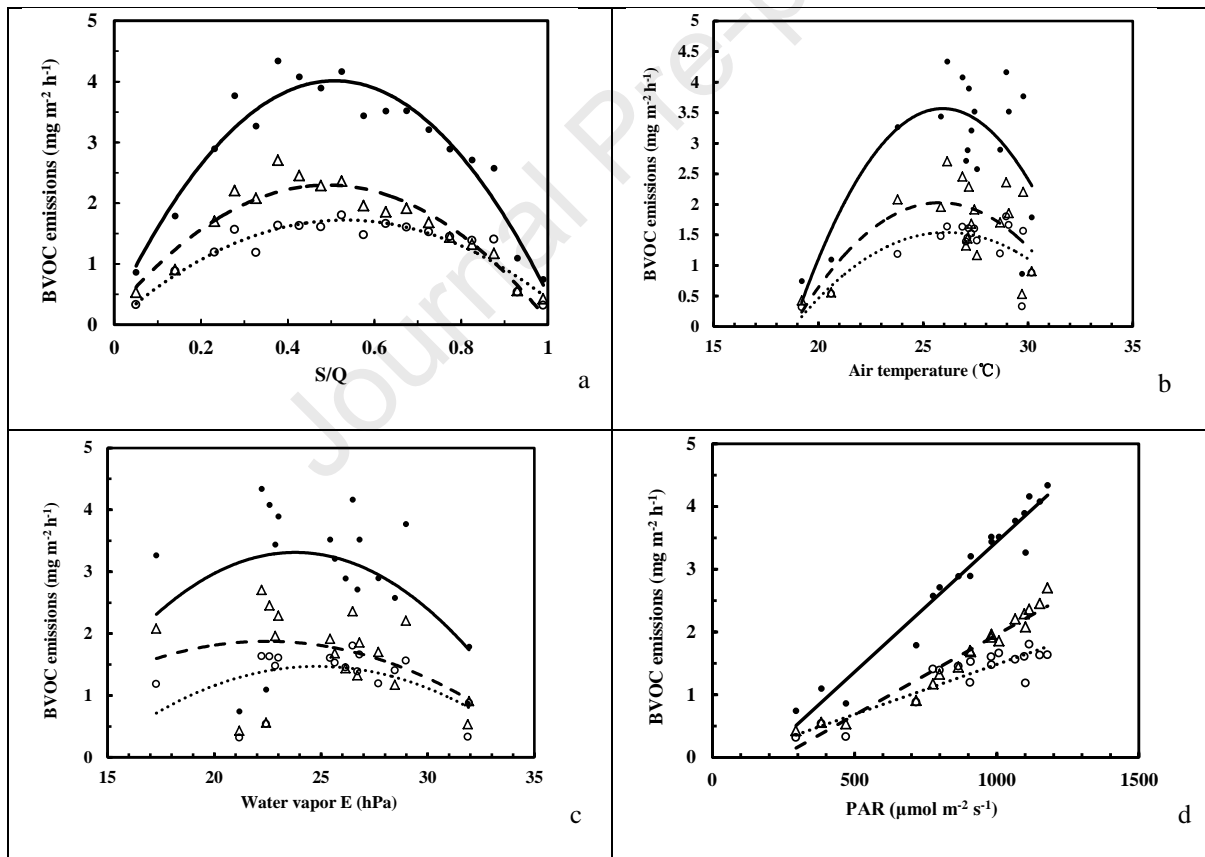


**Figure 12.** The relationships between calculated BVOC emission fluxes and (a) S/Q, (b) water vapor pressure, (c) air temperature and (d) PAR, where the data have been binned with respect to S/Q in intervals of 0.05 (S/Q = 0 - 1). Fluxes of isoprene, monoterpenes and BVOCs (isoprene + monoterpenes) are indicated by open circles, triangles and filled circles. (adapted from Bai, 2021a).

VOCs are important for the oxidizing capacity of the atmosphere and are precursors for the formation of new aerosol particles by nucleation. Kulmala et al. (2011) formulated proxies for the concentration in the nucleation mode in terms of the organic precursor vapor concentration ([ORG]), the ultraviolet radiation (UV) and the condensation sink (CS), i.e.  $N_{n,3} = UV [ORG]/CS^2$  and  $N_{n,4} = UV^2 [ORG]^2/CS^3$  for the estimation of the formation of new particles using satellite observations. The condensation sink is a measure for the aerosol surface available for condensation of vapors on existing aerosol particles in the atmosphere. However, the newly nucleated particles formed by nucleation are too small to serve as CS or to be observed from satellites directly and it takes time for them to grow into the accumulation mode (by condensation and coagulation) and thus provide enough surface area to be detected by optical instruments. The proxies show that an increase of BVOC emissions results in the production of small aerosol particles, but the non-linear behavior of the BVOC emissions will also affect the formation of new particles.

In view of the simultaneous increase of S/Q and BVOC emissions during favorable conditions, human-induced enhancement of BVOC emissions is recommended to be reduced to avoid increase of BVOC emissions and subsequent photochemical formation of fine particulates, e.g., by cutting plants and grasses in cities after 16:00 and by controlling biomass burning, in order to control O<sub>3</sub> and aerosol pollution (Bai, 2021b).

### 3.3 Time series and trends

Air pollution results from emissions of pollutants and unfavorable meteorological conditions. The air pollution can be reduced by reducing pollutant emissions by the implementation of policy measures. Time series of air pollutant concentrations show the effects of emission reduction policy, which however may be masked by meteorological conditions. Meteorological effects can be determined by comparison of observed and model-calculated time series, where in the model the emissions for the whole run are fixed to those in the starting year, but actual meteorological conditions are used. Hence the model shows only meteorological effects on the variation of the pollutant concentrations. This method is discussed in Section 3.3.1, for time series of aerosol concentrations, using AOD as a proxy, for 2010-2022. The method to determine the 2008-2022 CO trends over China using IASI observations is discussed in Section 3.3.2 and results are presented.

#### 3.3.1 Monitoring effects of emission reduction in China through AOD time series

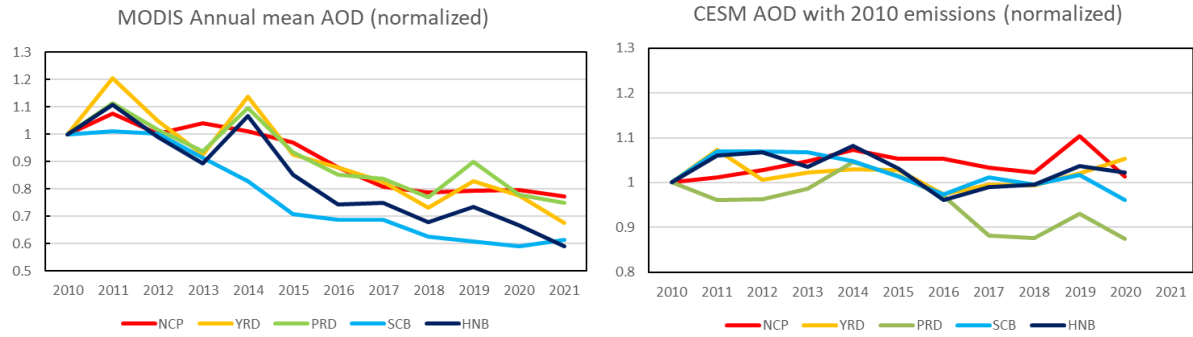
The atmospheric concentrations of aerosol and trace gases in China have been increasing during the 20<sup>th</sup> century. To reduce them and thus improve air quality, emission reduction measures have been implemented starting in the first decade of the 21<sup>st</sup> century, through a series of 5-Year Plans and Action Plans for Clean Air. These plans have resulted in the reduction of SO<sub>2</sub> since 2007 and NO<sub>2</sub> since 2011, as shown by van der A et al. (2017) using data from the Ozone Monitoring Instrument (OMI) flying on the Aura satellite. However, time series of annual mean AOD derived from MODIS Terra and Aqua observations using the Multi-Angle Implementation of Atmospheric Correction (MAIAC) algorithm Lyapustin et al. 2018), show that aerosol concentrations over most of eastern China started to decrease only from 2014 and this decrease flattened from about 2018, varying somewhat between different locations across China (de Leeuw et al., 2021; 2022). The flattening was first reported for two cities in China (Shanghai and Zhengzhou) (de Leeuw et al. 2021) and was confirmed from time series of AOD averaged over provinces in South-Eastern China Below the Hu line (SECBH) (de Leeuw et al. 2021). This study also showed that the AOD reached a maximum in 2014 over provinces in central China, but over provinces in the north or the south of the SECBH the AOD decrease started earlier.

To further investigate these AOD time series and determine whether the AOD variations were due to meteorological or anthropogenic influences, the satellite-derived AOD times were used together with methods outlined in Kang et al. (2019). Kang et al. used a chemistry-transport model to compute time series

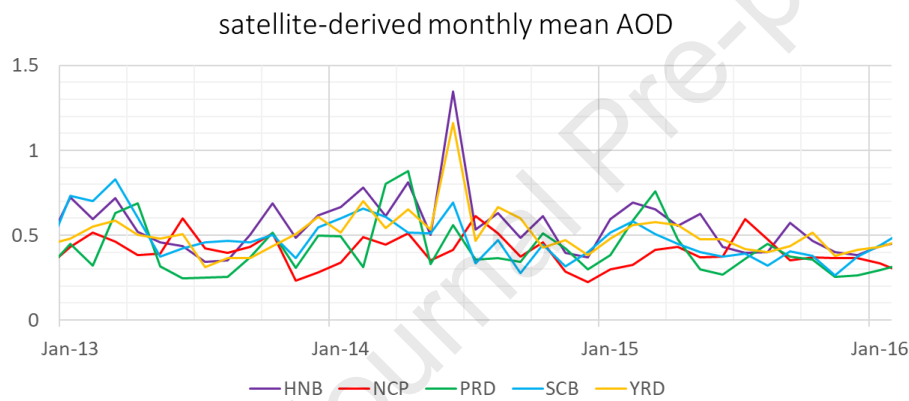
of AOD and trace gases, with actual meteorology but with emissions fixed to those in a reference year. In this way, all AOD variations are caused by meteorological influences and from the comparison with satellite observations, which include both meteorological and anthropogenic effects on the AOD, these effects can be separated and quantified. This was achieved by application of the Community Earth System Model (CESM) Version 1.0.4 (Hurrell et al., 2013) with the Community Atmospheric Model version 5 (CAM5) (Neale et al., 2012) for the simulation of aerosol concentrations. CESM has a spatial resolution of  $1.9^\circ \times 2.5^\circ$  (latitude  $\times$  longitude). The AOD was calculated from the modelled aerosol concentrations, for each grid point and time step, with the model developed by Zhang et al. (2017). The CESM was applied to provide AOD for the period January 2010 to August 2022, with emissions fixed to those for 2010 and with actual MERRA-2 (Modern Era Retrospective analysis for Research and Applications) re-analysis meteorological data (Rienecker et al., 2011; Gelaro et al., 2017). The CESM resolution does not allow for the application on a provincial scale and therefore five larger areas, representative of large industrial and urban centers in different climate, were selected for this study: the North China Plain (NCP), the Yangtze River Delta (YRD), the Pearl River Delta (PRD), the Sichuan Basin (SCB) and Hunan and Hubei (HNB).

Figure 13 shows the time series of the annual mean AOD over the 5 study regions retrieved from MODIS data using the MAIAC algorithm and obtained from the CESM simulations using fixed emissions and actual meteorology. The time series in Figure 13 have been normalized to the year 2010. The MODIS time series, extended with one year with respect to those of de Leeuw et al. (2022), shows the AOD peak in 2014 for YRD, PRD and HNB and the flattening of the decrease from about 2018, confirming earlier observations on the provincial scale. The CESM data show that the normalized simulated AOD is larger than 1, which can only be caused by meteorological effects on the AOD. This leads to the conclusion that meteorological effects played a role in the enhancement of the AOD in 2014 despite the implementation of the 2013-2017 Clean Air Action Plan aimed at reducing aerosol concentrations (Feng et al. 2019). Indeed, PM<sub>2.5</sub> concentrations strongly decreased between 2013 and 2017 as reported in many publications (e.g., Zheng et al., 2018a; Zhang et al., 2019a; Zhang et al., 2019b; Zhai et al., 2019; Feng et al., 2019; Xiao et al., 2021) and, unlike AOD, the annual average PM<sub>2.5</sub> concentrations do not peak in 2014 as shown in Figure 3 of Xiao et al. (2021). Xiao et al. (2021) derived PM<sub>2.5</sub> from MODIS AOD over key regions, some of which are similar to the ones used in our study. using models, ground-based PM<sub>2.5</sub> measurements and machine learning. Their algorithm appears to have effectively removed the anomaly in the AOD data, resulting in smooth PM<sub>2.5</sub> time series.

The year 2014 was anomalous, with winterhaze, summer drought and monsoon effects as reported in several studies (e.g., Cao et al., 2015; Wang and He, 2015; Yin et al., 2017; 2024). Most of these studies focused on the NCP where the observed AOD was not enhanced but the model simulations in Figure 13b show a substantial meteorologically induced increase. A similar increase is simulated over the HNB, but over the other three study areas the meteorological effect is smaller. In contrast, the observations in Figure 13a show a much larger increase over the YRD, the PRD and the HNB, in particular considering that the AOD had overall decreased from the start of the study in 2010. To further investigate these effects, time series of monthly averaged AOD observations in 2013-2015 were used (Figure 14). The data in Figure 14 show that in the first half of 2014 the AOD was enhanced over all five regions, with anomalously high peaks in June over the HNB and the YRD (monthly mean AOD  $\sim 1.2$  as compared to peak values of 0.6-0.8 in adjacent years). Over the HNB another peak is observed in April and over the PRD anomalously high AOD was observed in March and April. After June the AOD dropped to below  $\sim 0.6$  over all regions, but with NCP peaking in July. This behavior is in line with the large scale meteorological situations reported in Wang and He (2015), showing precipitation anomalies in July and August 2014 (high over central and south China, low over the north), and Yin et al. (2017). To further specify meteorological conditions influencing the AOD series in 2014 would require a detailed model study which is beyond the scope of this paper.



**Figure 13.** Time series of the annual mean AOD (January 2010- August 2022) over the 5 study regions (a) retrieved from MODIS data using the MAIAC algorithm, (b) obtained from the CESM simulations using fixed emissions and actual meteorology. All time series have been normalized to the year 2010.



**Figure 14.** Time series of satellite-derived monthly mean AOD (January 2010- August 2022) over the 5 study regions

The data in Figure 13 show that, for the years 2017-2021, the difference for each year from the average is  $\pm 10\%$ , confirming that the decrease flattened during these years. During this flattening period an AOD peak is observed over the YRD, the PRD, and the HNB in 2019. The satellite-derived monthly mean AOD data (not shown) reveal that anomalously high AOD occurred over the PRD in March and April 2019, over the YRD in these same months with an additional peak in July and over the HNB in March and in August/September. Also the model simulations show an AOD peak in 2019, over all areas except YRD where AOD continued to increase in 2020. These simulations suggest that meteorological effects contributed to the enhanced AOD and thus offset the effects expected from the implementation of the Three-year Action Plan for Clean Air in 2018. Like 2014, also the year 2019 was anomalously warm, in particular in the north and east of China, with anomalously high precipitation in central east China (Zeng et al., 2020). The reasons for the enhanced meteorologically-induced AOD increase requires a detailed analysis as indicated above for 2014.

### 3.3.2 IASI Satellite CO Trends (2008-2022)

Since 2007, three IASI (Infrared Atmospheric Sounding Interferometer) instruments have been successively embarked on board the polar-orbiting METeorological Operational satellites Metop-A, -B and -C. They provide daily global coverage of CO total column concentrations in the atmosphere with two daily overpasses (at 9:30 am and 9:30 pm, local time).

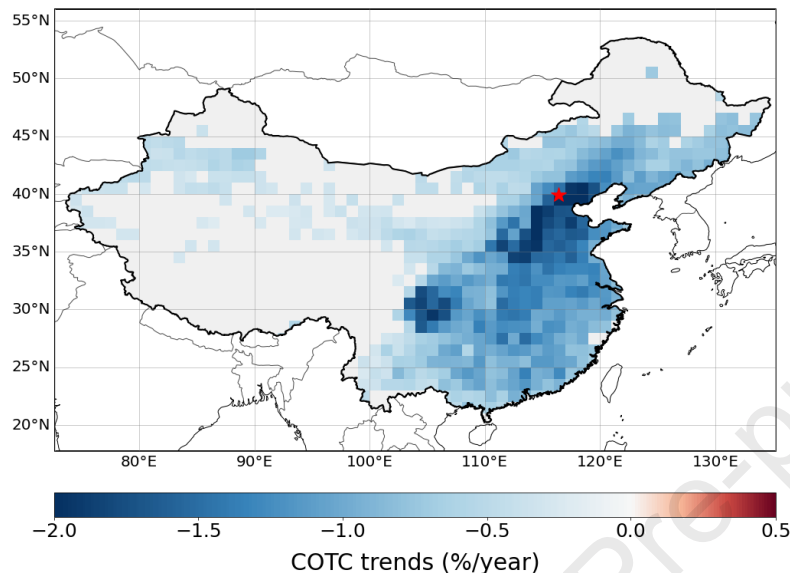


**Figure 15.** Carbon monoxide total columns (COTC) trends derived from IASI daytime gridded data (from January 2008 to December 2022, with  $1^\circ \times 1^\circ$  spatial resolution). Areas where the trends are not statistically significant ( $p > 0.05$ ) are indicated in grey. The location of Beijing is marked with a red star.

The map in Figure 15 shows the 2008–2022 trends in IASI carbon monoxide total columns (COTC) over China with a spatial resolution of  $1^\circ \times 1^\circ$  (daytime data only). In the statistical method used here, the seasonal component of the dataset was removed by subtracting the monthly COTC concentrations for each year from the monthly averages of the 15-year data. These concentration anomalies were then divided by the average concentrations of the dataset, providing normalized values. The Theil-Sen method was then applied to the normalized data in order to compute the median slope of the time series, while ignoring errors induced by outliers. The p-value of Sen’s Slope was determined using the Mann-Kendall test.

Figure 15 shows an overall decline of COTC which can be explained by the reduction of emissions from source sectors in China, such as iron and steel industries, residential sources, gasoline-powered vehicles, and construction materials industries (Zheng et al., 2018b). The largest negative trends are observed over areas with high population density, especially the Beijing-Tianjin-Hebei region (trends larger than  $-2\%/year$ ). Industrial areas with high population density, like the Sichuan Basin, also show a significant decrease of COTC, more than  $-1.5\%/year$ .

### 3.4 Process studies

The concentrations, emissions, and trends of pollutants in the atmosphere are the result of a wide variety of processes, including anthropogenic and natural emissions (Section 3.2), their reduction, and meteorological processes which were briefly discussed in the Introduction (Section 1). Experiments contributing to a better understanding of the vertical mixing of pollutants in the ABL are discussed in Section 3.4.1. The mechanism of removal of  $O_3$  due to uptake on aerosol particles and cloud droplets is discussed in Section 3.4.2. Wind and large-scale weather systems are important factors in the transport and removal of pollutants and their

vertical and spatial distribution. Validation of satellite-derived wind products is discussed in Section 3.4.3 and the effect of a large-scale weather system on the distribution of PM<sub>2.5</sub> is discussed in Section 3.4.4.

#### *3.4.1 Measurement of vertical in situ nitrogen dioxide profiles near Nanjing using a quadcopter*

NO<sub>2</sub> is a key component of air pollution worldwide. The Royal Netherlands Meteorological Institute (KNMI) Research and Development Satellite Observations department monitors trace gases such as NO<sub>2</sub> from space using satellite instruments such as TROPOMI. The amount of NO<sub>2</sub> in the atmosphere derived from TROPOMI observations is often divided into a tropospheric and a stratospheric amount. The derived tropospheric column density of NO<sub>2</sub> often is subjected to large uncertainties of about 30-40%. One of the major sources of uncertainty is the assumed NO<sub>2</sub> vertical profile shape in the troposphere. In addition to satellite validation, measurement of the vertical distribution of NO<sub>2</sub> is essential to: 1) Study NO<sub>x</sub> - photochemistry and (aerosol) dynamics; 2) Validate results from chemical models; 3) Understand effects of regional transport and 4) Identify sources and sinks (Wang et al., 2019). The objective of the current study is to determine the vertical distribution of NO<sub>2</sub> in the planetary boundary layer (PBL) and gain better insight into the local NO<sub>x</sub> photochemistry.

To achieve this objective, KNMI and the Nanjing University of Information Science and Technology (NUIST) conducted repetitive, high-resolution soundings of the PBL. These soundings were performed in Nanjing, Jiangsu, China, at a rural site in the Pukou district (32.214 °N, 118.658 °E) during the period 1-14 June 2018, using an in-house developed, accurate in-situ NO<sub>2</sub> sensor mounted on a quadcopter. The NO<sub>2</sub> sensor, called the KNMI NO<sub>2</sub>-sonde (Sluis et al., 2010), was calibrated by means of a side-by-side inter-comparison with a commercial Thermo Environmental Instruments (TEI) 42 type NO<sub>x</sub> analyzer installed at the nearby NUIST campus.

During the period 2-12 June 2018, 36 calibrated NO<sub>2</sub> vertical profiles were measured. This collection of profiles clearly shows the diurnal cycle of NO<sub>2</sub>. Elevated NO<sub>2</sub> concentrations close to the surface were observed during the night and the early morning, followed by development of the PBL from sunrise onward. During the afternoon, the PBL was well-mixed, and the vertical NO<sub>2</sub> concentration profiles showed little variation between the surface and the top of the PBL, but with much lower concentrations near the surface than during the night and early morning. This is clearly illustrated with the profiles measured on 5 June 2018 (Figure 16).

More accurate flight telemetry data from the unmanned aerial vehicle (UAV) could improve the vertical profile accuracy and resolution. However, because these were not available, simultaneously measured pressure data from the NUIST ozone sensor has been used to determine the height of the NO<sub>2</sub> observations. Furthermore, some of the nighttime measurements suffered from saturation issues i.e. the NO<sub>2</sub>-sensor could not always capture full night-time NO<sub>2</sub> peak concentrations. If available, a surface NO<sub>2</sub> dataset could be used to determine a possible correction factor. Finally, supplementary surface NO<sub>2</sub> data should also be used to investigate cases where the upward and downward soundings differ substantially and cases where the measured NO<sub>2</sub> volume mixing ratios appear too low.

In conclusion, with the KNMI NO<sub>2</sub>-sonde mounted on the NUIST quadcopter a unique dataset of 36 vertical in-situ NO<sub>2</sub> profiles was collected that demonstrates the (local) diurnal cycle. This data set will be further analyzed together with O<sub>3</sub>, PM<sub>2.5</sub> and black carbon (BC) profiles measured simultaneously on the quadcopter, as well as with NO<sub>2</sub> profiles measured at the nearby NUIST campus.

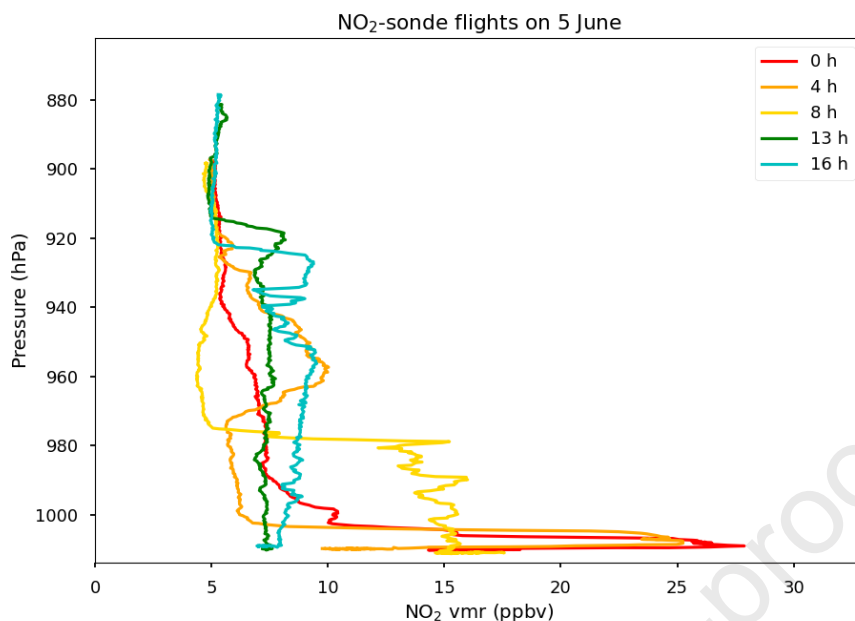


**Figure 16.** Overview of a typical measurement day where the diurnal cycle of NO<sub>2</sub> is clearly visible. 0 and 4 AM: elevated concentrations near the surface during the night and early morning; 8 AM: development of the PBL from sunrise onward. 1 and 4 PM: well-mixed PBL, flat NO<sub>2</sub> vertical profile shapes with lower concentrations.

### 3.4.2 Tropospheric ozone removal due to its diffusion in solid particles

The removal of tropospheric O<sub>3</sub> (TrO<sub>3</sub>) by aerosol and water droplets in Athens, Greece (38.0 °N, 23.70 °E) and Xuzhou, Jiangsu, China (34.2 °N, 117.1 °E) is estimated, based on the removal mechanisms and uptake rate as a function of accommodation and diffusional mechanisms.

The sticking efficiency or mass accommodation coefficient of a gas molecule impinging on a liquid surface indicates the probability that this molecule will enter the bulk liquid phase. The most widely used values for the mass accommodation coefficient are 1 and 0.036. However, the application of the model developed earlier by Ghosh et al. (2018) to data obtained in Athens and Xuzhou, led to the conclusion that these widely used values differ significantly from those found in this study, i.e., for water vapor impinging on cloud droplets, the values of the mass accommodation coefficient vary in the range 0.004 - 0.046. Using these values in the cloud droplet growth equations results in large changes in cloud base height position of up to 30%, suggesting that even large-scale models should use appropriate accommodation and diffusion coefficients.

In addition, the diffusion of gas-phase molecules of various atmospheric compounds into solid particles is governed by a vacancy-mediated mechanism. In this context, H<sub>2</sub>O ice particles play a key role in the TrO<sub>3</sub> loss. The relevant model developed by Varotsos and Zellner (2010) is mainly based on the following. When a single diffusion mechanism operates in a solid, the diffusion coefficient,  $D$ , of gas-phase molecules in a solid is often found to follow an Arrhenius-type behaviour, i.e.,  $D = D_0 \exp[-E/(k_B T)]$ , where the activation energy  $E$  and the pre-exponential factor  $D_0$  are essentially temperature independent, and  $k_B$  is the Boltzmann constant. The temperature-dependent measurements of  $D$  for various gas-phase molecules in solids have shown that their  $D_0$  values differ by several orders of magnitude, while their  $D$  values do not differ significantly. This indicates that material transport occurs at comparable rates for the same

mechanism. Despite this variation, a linear relationship between  $\ln Do$  and  $E$  holds. In the case of ice the following relationship applies:  $\ln Do = 2.5023 E - 20.365$ . If  $Do$  values could be estimated, then the above relationship could have substantial predictive power for the diffusion coefficients of other species, e.g.,  $O_3$  in ice.

Analysis of the ozone-sounding observations shows a significant anticorrelation between  $O_3$  concentration and water vapor mixing ratio, which becomes stronger on cloudy days. The result from this analysis is that in the upper PBL, the  $O_3$  uptake rates are high due to the preponderance of large cloud droplets, and this is reflected in the drop of  $O_3$  concentration observed in both the Athens and Xuzhou regions. At the gas-liquid interface, mass transfer is governed by molecular dynamics, while away from the droplet, surface eddy motions are responsible for mass transfer. To quantify  $O_3$  uptake by tropospheric clouds we used the model developed by Varotsos and Ghosh (2017), in which processes were considered within the gas phase and  $O_3$  transport in a cloud droplet proceeds by both molecular and turbulent diffusion. The results show that for the summer season, the diffusivity at the surface is lower than that at the top of the PBL by about 35%. Also, the summer and spring profiles show larger diffusivity values than the autumn and winter profiles, thus confirming the  $T^{3/2}$  law for diffusivity. In addition, the diffusional contribution to the  $O_3$  uptake rate increases with increasing droplet size in both Athens and Xuzhou.

### 3.4.3 Validation of Aeolus wind products using ground-based radar wind profiler network of China

Aeolus is the first satellite mission providing global wind profile information. The Atmospheric Laser Doppler Instrument (ALADIN) is a direct-detection ultraviolet wind lidar aboard Aeolus operating at 355 nm (Reitebuch, 2012; Ingmann and Straume, 2016). It is a dual channel design, with a Mie channel for the detection of aerosol backscatter and a Rayleigh channel for the detection of molecular backscatter, operating simultaneously. The wind speed is calculated from the signals in each channel based on the Doppler effect, after application of atmospheric and bias corrections. Aeolus provides wind profiles from the surface up to 30 km, i.e., the wind vector component along the instrument's line of sight, with a vertical resolution of 0.25 to 2 km and a wind accuracy of 2 to 4 m/s, depending on altitude. The Aeolus data products were released to the public on 12 May 2020. However, before they can be used operationally in scientific studies or industrial applications, the Aeolus wind products need to be extensively evaluated by comparison with data from ground-based remote sensing measurements.

In the current study, Aeolus L2B products containing horizontal line of sight (HLOS) wind components, have been evaluated over China for the period from 20 April to 20 July 2020. Rayleigh-clear winds, referring to the wind observations in an aerosol-free atmosphere, and Mie-cloudy winds, acquired from Mie backscatter signals induced by aerosols and clouds, have been validated using wind observations from the radar wind profiler (RWP) network in China as a reference. The Aeolus and RWP were collocated according to three matchup criteria, with 1 or 2 overpasses within 37.5 km of the RWP site and the third one with 1 overpass at a distance between 37.5 and 75 km of the RWP site. The evaluation shows that the performance of the Mie-cloudy wind products does not change much between the three matchup categories, but for the Rayleigh-clear wind products, the differences for the first two categories are much smaller than for category 3 where the distance between the Aeolus overpass and the RWP site is larger. The vertical variations of the Aeolus wind products are similar to those of the RWP observations, except for the Rayleigh-clear winds in the height range of 0–1 km, due to the limited power in the Rayleigh channel at these altitudes. The mean absolute normalized differences between the Mie-cloudy (Rayleigh-clear) and the RWP wind components are 3.06 (5.45) for all orbits, 2.79 (4.81) for ascending orbits and 3.32 (5.72) m/s for descending orbits. This indicates that the wind products for ascending orbits are slightly better than those for descending orbits, and the observation time has a minor effect on the comparison. The Aeolus Mie-cloudy winds are consistent with the RWP winds over most of east China, except in coastal areas where the Aeolus Rayleigh-clear winds are more reliable. Overall, the Mie-cloudy (Rayleigh-clear) and RWP winds correlate well, with correlation coefficients  $R$  of 0.94 (0.81). These results show the good

agreement of the Aeolus wind products with wind observations from the RWP network in China, which provides sufficient confidence that the newly released Aeolus wind products can be used for assimilation in operational weather forecasting in China (Guo et al., 2021a).

#### 3.4.4 Characterization of the role of atmospheric turbulence and stratification in aerosol pollution

Fine particulate matter (PM<sub>2.5</sub>) concentrations near the surface can be significantly modulated by atmospheric turbulence (Xia et al., 2022) and the stratification of the PBL. However, the mechanism by which these factors influence the variation in PM<sub>2.5</sub> remains poorly understood. To better understand the influence of turbulence and PBL stratification on PM<sub>2.5</sub>, surface-based meteorological and PM<sub>2.5</sub> observations, turbulent kinetic energy from a sonic anemometer (Figure 17a), and high-resolution soundings have been analyzed during a severe regional pollution transport event in Xiangyang (32.0090 °N, 112.1226 °E), a city in the middle reaches of the Yangtze River, from January 3 to January 9, 2019. To the north lies a large plain region (Figure 17), which is subjected to the long-range transport of atmospheric pollutants from the north. During this period, Xiangyang was influenced by a developing Mongolian high-pressure system moving eastward, resulting in a northerly airflow over Central China favorable for the transboundary transport of pollutants to Xiangyang on January 4 and 5 when PM<sub>2.5</sub> was continuously increasing. During the next few days, the Mongolian high-pressure system continued to develop and moved further eastward and southward, resulting in the accumulation of pollutants in the Xiangyang area on January 6. Afterwards, the Mongolian high moved further eastward and southward and then weakened. Central China was controlled by northerly airflow at the bottom of the high-pressure system and easterly airflow behind the system. The atmospheric pollution event gradually weakened and disappeared.

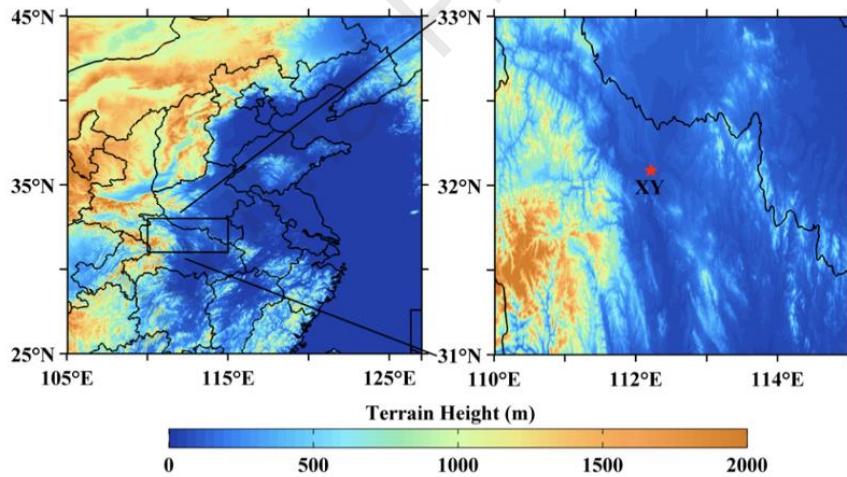


**Figure 17.** The terrain map of Xiangyang (XY marked with a red star in the upper right panel), a city in central China. Also shown is the weather station of XY and its surrounding environment (lower left panel), in which a 3-D Sonic Anemometer (CSAT3) manufactured by Campbell Scientific is installed. The tethered balloon launched from the roof of Xiangyang weather station was mainly used for measuring PM<sub>2.5</sub> at various altitudes (lower right panel).

During the entire pollution event, the turbulent kinetic energy and sensible heat flux tended to be lower at high PM<sub>2.5</sub> concentrations and there was no obvious inversion layer below 500 m. During the initial and maintenance stages, there was a negative correlation between the turbulent kinetic energy or sensible heat flux and PM<sub>2.5</sub>, while the correlation was positive during the growth stage when regional transport dominated the variation in PM. During the initial and maintenance stages, a weak inversion layer appeared at higher altitudes. The occurrence of low PM<sub>2.5</sub> concentrations within the atmospheric surface layer, observed by the tethered balloon (Figure 17), is explained by the presence of wind shear during the prevailing northerly winds. The pollutants were transported from the north over large distances but the wind shear prevented their downward transport. For more detail, see Zhou et al. (2022) and Guo et al. (2021b).

#### 4. Discussion and conclusions

The focus of this work is on the use of satellite remote sensing to improve our understanding of air quality in China. Air quality aspects addressed are the emission of BVOCs in a rural area, building on earlier studies in other areas with different types of vegetation (Section 3.2.4), and the effect of large weather systems on PM<sub>2.5</sub> using sophisticated instrumentation to understand the processes involved (Section 3.4.4). The latter includes the use of high-resolution soundings of PM<sub>2.5</sub> and influencing parameters measured from a tethered balloon. To study NO<sub>2</sub> profiles, a quadcopter was used, carrying a sophisticated in-house built NO<sub>2</sub> sensor together with a few other instruments for measuring O<sub>3</sub> and black carbon profiles and a pressure sensor as an indicator of the elevation above the surface (Section 3.4.1). Another process studied was the removal of tropospheric O<sub>3</sub> by aerosol and water droplets to explain the anticorrelation between O<sub>3</sub> concentration and the water vapor mixing ratio observed by ozone soundings (Section 3.4.2). This is due to high O<sub>3</sub> uptake rates in the presence of large cloud droplets in the upper planetary boundary layer, which results in the drop of O<sub>3</sub> concentration observed in both the Athens and Xuzhou regions.

Other teams focus on the development of algorithms to improve the information retrieved from satellite observations, such as the use of polarization to increase the number of degrees of freedom for more accurate retrieval of aerosol parameters, in particular AOD (Section 3.1.1). The increased information content is also used, together with dedicated models, to improve the AOD/PM<sub>2.5</sub> relationship and retrieve PM<sub>2.5</sub> as demonstrated with PCF synthetic data. Such studies lead to a better understanding of how satellite observations of AOD can be used for AQ studies which require PM<sub>2.5</sub> (Section 3.1.2). These studies are made using polar orbiting satellites flying in a low Earth orbit (LEO), which at low latitudes provide at best a single overpass per day during daylight hours. Complementary to this effort, instruments on geostationary (GEO) satellites are being used to develop algorithms for AOD retrieval, providing high temporal resolution which can be used to provide information on the diurnal variation of aerosols and the evolution of air quality. The improvement in spatial resolution to a scale of the order of 100 m renders the data better suited to study small-scale variations in urban areas (Section 3.1.4). All such studies require validation. Ground-based networks have been established and are maintained and expanded to provide high-quality reference data for aerosol retrieval, such as from the Chinese SONET sun photometer network, complementary to the global AERONET (Section 3.1.3), and the radar wind profiler (RWP) network in China used as a reference for the validation of Aeolus wind products (Section 3.4.3).

Much work is focused on the retrieval of NO<sub>2</sub> from satellite data, in particular on the use of OMI and TROPOMI data. The validation of TROPOMI retrieval results, using MAX-DOAS data at Xuzhou as a

reference, is addressed in Section 3.1.5 and the data set was used in studies on the diurnal variation of  $\text{NO}_2$  and on the importance of spatial scales. TROPOMI  $\text{NO}_2$  data were used to determine  $\text{NO}_2$  emissions over the Yangtze River Delta using the DECSO model (Section 3.2.1) with a resolution of  $0.1^\circ \times 0.1^\circ$ , showing the high emissions along the Yangtze River as well as from large urban centers.  $\text{NO}_x$  emissions retrieved along the Yangtze River were subsequently used to compile a novel inventory of emissions from ships sailing on the river in the region of Nanjing. The results show the substantial contribution of ship emissions to the total  $\text{NO}_2$  emission in that area (Section 3.2.2). The  $\text{NO}_x$  and  $\text{CO}_2$  emissions from a large anthropogenic source, taking the Megacity Wuhan as an example, were determined using TROPOMI data together with  $\text{CO}_2:\text{NO}_x$  emission ratios from two emission inventories and an improved superposition model driven by satellite  $\text{NO}_2$  measurements and verified by satellite  $\text{CO}_2$  measurements (Section 3.2.3). TROPOMI  $\text{NO}_2$  data, combined with the Vaisala Global Lightning Dataset, were used to determine the production of  $\text{NO}_x$  from lightning over the Arctic during the summer months. The results were compared with other  $\text{NO}_x$  sources at latitudes within the Arctic Circle, and the importance of this source has been discussed (Section 3.1.6).

The implementation of emission reduction measures to improve AQ requires monitoring the effect of these measures on the concentrations of aerosols and trace gases. Preferably, ground-based networks would be used, providing a long time series of concentrations where they matter most for AQ. However, as mentioned in the introduction, in China such networks were established in 2013 and thus do not provide prior information, while also gaps exist in the spatial coverage. Satellite observations providing continuous time series of AOD go back to 1995 (Along Track Scanning Radiometer 2, ATSR-2, which flew on ENVISAT), and comparison of ATSR-retrieved AOD time series over SE China with those published in Sogacheva et al. (2018) shows that in 2017 the AOD was close to that in 1995 (de Leeuw et al., 2021). Provincial scale time series show large fluctuations, with a decrease starting between 2011 and 2014 (depending on the location in China), which flattened in recent years (from about 2018). Comparison with model simulations discussed in Section 3.3.1 shows the substantial influence of meteorological factors which either reduce or reinforce the effects of emission reduction. The decrease of CO over China, for the period 2008-2022, was studied using CO total column concentrations (COTC) retrieved from IASI on METOP-A, B, and C, with a spatial resolution of  $1^\circ \times 1^\circ$  (daytime data only) (Section 3.3.2). The results show an overall decline of COTC, with the highest negative trends (more than  $-2\%/year$ ) over areas with high population density, especially the Beijing-Tianjin-Hebei region and the Sichuan Basin.

In conclusion, the use of satellite remote sensing has considerably contributed to improving our understanding of the mechanisms and processes affecting air quality in China and has provided several new products:

- A new AOD data set, using polarization data from the polarized scanning atmospheric corrector (PSAC).
- AOD/PM<sub>2.5</sub> ratios and PM<sub>2.5</sub> data retrieved using data from the Polarization CrossFire (PCF) satellite, together with the PMRS model.
- A high-resolution AOD data set for urban air pollution monitoring using GF-1 data together with MODIS AOD data.
- Validated satellite-retrieved wind products over China.
- Production efficiency and lifetime of  $\text{NO}_2$  from lightning in the Arctic during the summer seasons of 2019–2021.
- A high-resolution  $\text{NO}_x$  emission data base over the Yangtze River Delta derived from TROPOMI data.
- An estimate of the impact of inland ship emissions on air quality in the region of Nanjing.
- A new tool for quantification of city-scale emissions of  $\text{NO}_x$  and  $\text{CO}_2$ , driven by satellite  $\text{NO}_2$  measurements.

- A data set for the analysis of the vertical variation of NO<sub>2</sub>, using dedicated equipment on a quadcopter.
- A characterization of the role of atmospheric turbulence and stratification in aerosol pollution.
- Information on the role of aerosol and cloud droplets in the removal of tropospheric O<sub>3</sub>, explaining observations on the variation of O<sub>3</sub> over Athens and Xuzhou.
- Information on the sensitivity of BVOC emissions to influencing factors such as PAR, air temperature, water vapor pressure, and atmospheric pollution.

The AOD time series and CO trends lead to the conclusion that the emission reduction policy in China has been effective but, as shown from the AOD time series, meteorological effects need to be accounted for to further reduce aerosol concentrations.

The analysis of the importance of the production of NO<sub>2</sub> from lightning in relation to other sources suggests that LNO<sub>2</sub> can play an important role in the upper troposphere/lower stratosphere atmospheric chemical processes in the Arctic region, particularly during the summer.

The improved superposition model is a promising new tool for quantification of city-scale emissions of NO<sub>x</sub> and CO<sub>2</sub> allowing policymakers to gain rapid insights into spatial-temporal emission patterns and the effectiveness of carbon and nitrogen regulation in urban environments.

In summary, the cooperation between scientists with different backgrounds, interests and skills in the DRAGON5 project EMPAC has facilitated further insights in the use of satellite data for air quality studies and the effects of emission reduction policies on the concentrations. New sensors are being developed and deployed providing better quality with improved spatial and temporal resolution. Ground-based remote sensing reference data is crucial for the continuous validation and evaluation of satellite data. In situ data are used together with satellite data to develop better understanding of processes influencing atmospheric composition, including effects of emission reduction of one or more constituents on the evolution of others. In particular the influence of emission reduction policy on the oxidative capacity of the atmosphere is an important issue. Simulations of atmospheric processes using transport and climate models are of utmost importance to understand the satellite observations, to develop and improve the algorithms applied to analyze the satellite observations and to separate different effects on the observed variations. The analysis leads to important conclusions on the implication of emission reduction policies and thus improve air quality.

In the current study we have mainly used data from sensors on polar orbiting satellites, with some examples from the geostationary Himawari satellite. With the launch of GEMS and other sensors on geostationary satellites (TEMPO, Sentinel-4), important AQ data will become available with high temporal resolution providing detailed information on the evolution of trace gases and aerosols over very large areas. This creates enormous amounts of data which requires the application of machine learning (ML) techniques for the fast processing needed to timely make these data available. ML strongly depends on the availability of reliable data sets for training and excellent results have been achieved. For the detailed understanding of atmospheric phenomena, the combination of detailed in situ measurements, including laboratory studies, field campaigns and monitoring, modeling on a variety of scales and ground-based and satellite remote sensing are crucial, in particular in a rapidly changing environment such as China.

#### **Author Contributions**

Conceptualization: GdL, RvdA and JB; methodology: GdL, RvdA, JB, JG, ZL, YZ, KQ, SS, CV, YX, YY, XZ; software, RvdA, JB, MdH, CF, JD, KQ, SS, QZ, XZ, XYZ, XZ; validation: all co-authors; formal analysis, all co-authors; investigation, all co-authors; resources, GdL, RvdA, JB, JG, ZL, KQ, SS, CV, YX, YY, XZ; data curation: RvdA, JB, MdH, YZ, CF, JD, KQ, SS, QZ, XZ, XYZ, XZ; writing—original draft preparation, GdL, RvdA, JB; review and editing, all co-authors.; visualization, all co-authors; supervision, GdL, RvdA, JB, JG, ZL, KQ, SS, CV, YX, YY, XZ; project administration, RvdA, JB; funding acquisition:

GdL, RvdA, JB, JG, ZL, KQ, SS, CV, YX, YY, XZ. All authors have read and agreed to the published version of the manuscript.

### Conflict of Interest

The authors declare no conflict of interest.

**Funding:** The EMPAC project is supported by the European Space Agency ESA, Contract No. 4000135384/21/I-NB. The project supports the young scientist position of Mirjam den Hoed at KNMI. Other young scientists working in the project are Xin Zhang and Xiumei Zhang (both at NUIST) and Selviga Sinnathamby (LATMOS). *The work on spaceborne observations of lightning NO<sub>2</sub> in the Arctic was funded by the National Natural Science Foundation of China (grant nos. 91644224 and 42075176).* The work on the impact of inland ship emissions on air quality was funded by the National Natural Science Foundation of China (grant nos. 42075176) and the program of China Scholarship Council (no. 202109040001). For the final preparation of this MS, Gerrit de Leeuw was supported by the Chinese Academy of Sciences President's International Fellowship Initiative. Grant No. 2025PVA0014.

### Acknowledgments

The study contributes to the EMPAC (Exploitation of satellite remote sensing to improve our understanding of the Mechanisms and Processes affecting Air quality in China) project which is part of the ESA/ NRSCC MOST cooperation project Dragon 5, Topic 3 Atmosphere, sub-topic 3.2 Air-Quality, project ID 59013. Gerrit de Leeuw is supported by the Chinese Academy of Sciences President's International Fellowship Initiative. Grant No. 2025PVA0014

### References

- Aan de Brugh, J. M. J., Henzing, J. S., Schaap, M., Morgan, W. T., van Heerwaarden, C. C., Weijers, E. P., Coe, H., Krol, M. C., 2012. Modelling the partitioning of ammonium nitrate in the convective boundary layer, *Atmos. Chem. Phys.*, 12, 3005–3023, <https://doi.org/10.5194/acp-12-3005-2012>, 2012.
- AERONET, 2024. Aerosol Robotic Network, <https://aeronet.gsfc.nasa.gov/> (last visited 30 June, 2024).
- Bai, J.H., 2021a. The relationships between BVOC emission fluxes and their influencing factors in a subtropical *Pinus* forest. *Ecology and Environmental Sciences*, 30(5), 889-897. DOI:10.16258/j.cnki.1674-5906.2021.05.001.
- Bai, J.H., 2021b. O<sub>3</sub> Concentration and its relation with BVOC emissions in a subtropical plantation. *Atmosphere*, 12, 711. <https://doi.org/10.3390/atmos12060711>.
- Bai J.H., Duhl, T., 2021. A primary generalized empirical model of BVOC emissions for some typical forests in China, *Atmospheric Pollution Research*. 12, 101126. doi: <https://doi.org/10.1016/j.apr.2021.101126>.
- Bai, R., Xue, Y., Jiang, X., Jin, C., Sun, Y., 2022. Retrieval of High-Resolution Aerosol Optical Depth for Urban Air Pollution Monitoring. *Atmosphere*, 13, 756. <https://doi.org/10.3390/atmos13050756>.
- Brunekreef, B., Holgate, S.T., 2002. Air pollution and health. *Lancet* 360: 1233–42. [https://doi.org/10.1016/S0140-6736\(02\)11274-8](https://doi.org/10.1016/S0140-6736(02)11274-8)
- Cao, Z., Sheng, L. Liu, Q., Yao, X., Wang, W., 2015. Interannual increase of regional haze-fog in North China Plain in summer by intensified easterly winds and orographic forcing. *Atm. Env.* 122, 154-162. <http://dx.doi.org/10.1016/j.atmosenv.2015.09.042>.

- Chen, T., Guestrin, C., 2016. XGBoost: A Scalable Tree Boosting System. Proceedings of the 22nd ACM SIGKDD International Conference on Knowledge Discovery and Data Mining, 785–794. <https://doi.org/10.1145/2939672.2939785>
- Curci, G., Ferrero, L., Tuccella, P., Barnaba, F., Angelini, F., Bolzacchini, E., Carbone, C., Denier van der Gon, H. A. C., Facchini, M. C., Gobbi, G. P., Kuenen, J. P. P., Landi, T. C., Perrino, C., Perrone, M. G., Sangiorgi, G., Stocchi, P., 2015. How much is particulate matter near the ground influenced by upperlevel processes within and above the PBL? A summertime case study in Milan (Italy) evidences the distinctive role of nitrate, *Atmos. Chem. Phys.*, 15, 2629–2649, <https://doi.org/10.5194/acp15-2629-2015>, 2015.
- de Leeuw, G., van der A, R.J., Bai, J., Xue, Y., Varotsos, C., Li, Z., Fan, C., Chen, X., Christodoulakis, I., Ding, J., Hou, X., Kouremadas, G., Li, D., Wang, J., Zara, M., Zhang, K., Zhang, Y., 2021. Air Quality over China. *Remote Sens.* 2021, 13, 3542. <https://doi.org/10.3390/rs13173542>.
- de Leeuw, G., Fan, C, Li, Z., Dong, J., Li, Y., Ou, Y., Zhu, S., 2022. Spatiotemporal variation and provincial scale differences of the AOD across China during 2000–2021. *Atmospheric Pollution Research* 13, 101359 (14 pp). <https://doi.org/10.1016/j.apr.2022.101359>.
- Ding, J., van der A, R. J., Eskes, H. J., Mijling, B., Stavrou, T., van Geffen, J. H. G. M., Veefkind, J.P., 2020. NO<sub>x</sub> emissions reduction and rebound in China due to the COVID-19 crisis. *Geophysical Research Letters* 46, 9 pp., e2020GL089912. <https://doi.org/10.1029/2020GL089912>.
- Dong, C., Loy, C. C., He, K., Tang, X. 2014. Learning a Deep Convolutional Network for Image Super-Resolution. *Computer Vision – ECCV 2014*, 8692, 184–199. [https://doi.org/10.1007/978-3-319-10593-2\\_13](https://doi.org/10.1007/978-3-319-10593-2_13)
- Earthdata, 2024. <https://www.earthdata.nasa.gov/learn/articles/geostationary-in-worldview> (last accessed 30 June 2024).
- eoPortal, 2024. Satellite mission catalogue. <https://www.eoportal.org/satellite-missions/gaofen-1#performance-specifications> (last accessed 30 June 2024).
- EPA, 2024a. United States Environmental Protection Agency, <https://www.epa.gov/eco-research/ecosystems-and-air-quality> (last accessed 30 June 2024).
- EPA, 2024b. United States Environmental Protection Agency, <https://www.epa.gov/sciencematters/tempo-new-era-air-quality-monitoring-space>, (last accessed 30 June 2024).
- EUMETSAT, 2024. <https://www.eumetsat.int/sentinel-4> (last accessed 30 June 2024).
- Fan, H.; Zhao, C.; Yang, Y., 2020a. A comprehensive analysis of the spatio-temporal variation of urban air pollution in China during 2014–2018. *Atmos Environ* 220, 117066, doi:<https://doi.org/10.1016/j.atmosenv.2019.117066>.
- Fan, C.; Li, Y.; Guang, J.; Li, Z.; Elnashar, A.; Allam, M.; de Leeuw, G., 2020b. The Impact of the Control Measures during the COVID-19 Outbreak on Air Pollution in China. *Remote Sensing* 12, 1613, <https://doi.org/10.3390/rs12101613>.
- Fan, C., Li, Z., Li, Y., Dong, J., van der A, R., de Leeuw, G., 2021. Variability of NO<sub>2</sub> concentrations over China and effect on air quality derived from satellite and ground-based observations, *Atmos. Chem. Phys.*, 21, 7723–7748, <https://doi.org/10.5194/acp-21-7723-2021>.
- Feng, Y., Ning, M., Lei, Y., Sun, Y., Liu, W., Wang, J., 2019. Defending blue sky in China: Effectiveness of the “Air Pollution Prevention and Control Action Plan” on air quality improvements from 2013 to 2017. *J. of Env. Management* 252, 109603, 13 pp. <https://doi.org/10.1016/j.jenvman.2019.109603>.

GCOS, 2024. Global Climate Observing System, <https://gcos.wmo.int/en/essential-climate-variables/precursors> (last accessed 30 June 2024).

Gelaro, R., McCarty, W., Suárez, M.J., Todling, R., Molod, A., Takacs, L., Randles, C., Darmenov, A., Bosilovich, M.G., Reichle, R., Wargan, K., Coy, L., Cullather, R., Draper, C., Akella, S., Buchard, V., Conaty, A., da Silva, A., Gu, W., Kim, G.K., Koster, R., Lucchesi, R., Merkova, D., Nielsen, J.E., Partyka, G., Pawson, S., Putman, W., Rienecker, M., Schubert, S.D., Sienkiewicz, M., Zhao, B., 2017. The Modern-Era Retrospective Analysis for Research and Applications, Version 2 (MERRA-2). *J Clim.* 30, 5419-5454. doi: 10.1175/JCLI-D-16-0758.1.

Ghosh, S., Gumber, S., Varotsos, C., 2018. A sensitivity study of diffusional mass transfer of gases in tropical storm hydrometeors. *Theoretical and Applied Climatology*, 134(3), 1083-1100, <https://doi.org/10.1007/s00704-017-2321-4>.

Guo, J., Liu, B., Gong, W., Shi, L., Zhang, Y., Ma, Y., Zhang, J., Chen, T., Bai, K., Stoffelen, A., de Leeuw, G., Xu, X., 2021a. Technical note: First comparison of wind observations from ESA's satellite mission Aeolus and ground-based radar wind profiler network of China. *Atmos. Chem. Phys.*, 21, 2945–2958, <https://doi.org/10.5194/acp-21-2945-2021>.

Guo, J., Zhang, J., Yang, K., Liao, H., Zhang, S., Huang, K., Lv, Y., Shao, J., Yu, T., Tong, B., Li, J., Su, T., Yin, S. H. L., Stoffelen, A., Zhai, P., Xu, X., 2021b. Investigation of near-global daytime boundary layer height using high-resolution radiosondes: First results and comparison with ERA-5, MERRA-2, JRA-55, and NCEP-2 reanalyses, *Atmos. Chem. Phys.*, 21, 17079–17097, <https://doi.org/10.5194/acp-21-17079-2021>.

Holben, B.N., Eck, T.F., Slutsker, I., Tanré, D., Buis, J.P., Setzer, A., Vermote, E., Reagan, J.A., Kaufman, Y.J., Nakajima, T., Lavenu, F., Jankowiak, I., Smirnov, A., 1998. Aeronet – a federated instrument network and data archive for aerosol characterization. *Remote Sens. Environ.* 66, 1–16. [https://doi.org/10.1016/S0034-4257\(98\)00031-5](https://doi.org/10.1016/S0034-4257(98)00031-5).

Hou, X., Zhu, B., Kumar, K. R., de Leeuw, G., Lu, W., Huang, Q., Zhu, X., 2020. Establishment of conceptual schemas of surface synoptic meteorological situations affecting fine particulate pollution across eastern China in the winter. *Journal of Geophysical Research: Atmospheres*, 125, e2020JD033153. <https://doi.org/10.1029/2020JD033153>.

Huang, X., Ding, A., Gao, J., Zheng, B., Zhou, D., Qi, X., Tang, R., Wang, J., Ren, C., Nie, W., 2020. Enhanced secondary pollution offset reduction of primary emissions during COVID19 lockdown in China. *National Science Review*, 8, nwaa137, <https://doi.org/10.1093/nsr/nwaa137>.

Hurrell, J.W., Holland, M.M., Gent, P.R., Ghan, S., Kay, J.E., Kushner, P.J., Lamarque, J.-F., Large, W.G., Lawrence, D., Lindsay, K., Lipscomb, W.H., Long, M.C., Mahowald, N., Marsh, D.R., Neale, R.B., Rasch, P., Vavrus, S., Vertenstein, M., Bader, D., Collins, W.D., Hack, J.J., Kiehl, J., Marshall, S., 2013. The Community Earth System Model: A Framework for Collaborative Research. *Bulletin of the American Meteorological Society*, 94(9), 1339-1360. <https://doi.org/10.1175/BAMS-D-12-00121.1>.

JMA, 2024. Japan Meteorological Agency, Meteorological Data Center <https://www.data.jma.go.jp/mscweb/data/himawari/> (last accessed 30 June 2024).

Ingmann, P., Straume, A. G., 2016. ADM-Aeolus Mission Requirements Document, ESA EOP-SM/2047, 57 pp., available at: [http://esamultimedia.esa.int/docs/EarthObservation/ADM-Aeolus\\_MRD.pdf](http://esamultimedia.esa.int/docs/EarthObservation/ADM-Aeolus_MRD.pdf) (last access: 30 June 2024).

Kahn, R. A., Gaitley, B. J., 2015. An analysis of global aerosol type as retrieved by MISR, *J. Geophys. Res. Atmos.*, 120, 4248–4281, doi:10.1002/2015JD023322.

Kang, H., Zhu, B., van der A, R.J., Zhu, C., de Leeuw, G., Hou, X., Gao, J., 2019. Natural and anthropogenic contributions to long-term variations of SO<sub>2</sub>, NO<sub>2</sub>, CO, and AOD over East China. *Atmospheric Research* 215, 284–293; <https://doi.org/10.1016/j.atmosres.2018.09.012>.

Kang, H., Zhu, B., de Leeuw, G., Yu, B., van der A, R. J., Lu, W., 2022. Impact of urban heat island on inorganic aerosol in the lower free troposphere: a case study in Hangzhou, China, *Atmos. Chem. Phys.*, 22, 10623–10634, <https://doi.org/10.5194/acp-22-10623-2022>, 2022.

Kulmala, M., Arola, A., Nieminen, T., Riuttanen, L., Sogacheva, L., de Leeuw, G., Kerminen, V.-M., Lehtinen, K. E. J., 2011. The first estimates of global nucleation mode aerosol concentrations based on satellite measurements, *Atmos. Chem. Phys.*, 11, 10791–10801, doi:10.5194/acp-11-10791-2011.

Li, Y., Xue, Y., He, X., Jie, G., 2012. High-resolution aerosol remote sensing retrieval over urban areas by synergetic use of HJ-1 CCD and MODIS data. *Atmos. Environ.*, 46, 173–180, <https://doi.org/10.1016/j.atmosenv.2011.10.002>.

Li, M., Liu, H., Geng, G., Hong, C., Liu, F., Song, Y., Tong, D., Zheng, B., Cui, H., Man, H., Zhang, Q., He, K., 2017. Anthropogenic emission inventories in China: a review, *Natl. Sci. Rev.*, 4, 834–866, <https://doi.org/10.1093/nsr/nwx150>.

Li, Z. Q., Xu, H., Li, K. T., Li, D. H., Xie, Y. S., Li, L., Zhang, Y., Gu, X. F., Zhao, W., Tian, Q. J., Deng, R. R., Su, X. L., Huang, B., Qiao, Y. L., Cui, W. Y., Hu, Y., Gong, C. L., Wang, Y. Q., Wang, X. F., Wang, J. P., Du, W. B., Pan, Z. Q., Li, Z. Z., Bu, D., 2018. Columnar Atmospheric Aerosols over China: An Overview of Sun–Sky Radiometer Observation Network (SONET) Measurements. *Bulletin of the American Meteorological Society*, 99(4), 739–755, <https://doi.org/10.1175/BAMS-D-17-0133.1>.

Li, L., Dubovik, O., Derimian, Y., Schuster, G. L., Lapyonok, T., Litvinov, P., Ducos, F., Fuertes, D., Chen, C., Li, Z., Lopatin, A., Torres, B., Che, H., 2019. Retrieval of aerosol components directly from satellite and ground-based measurements, *Atmos. Chem. Phys.*, 19, 13409–13443, <https://doi.org/10.5194/acp-19-13409-2019>.

Li, H., Liu, G., Han, C., Yang, Y., Chen, R., 2022a. Quantifying the Trends and Variations in the Frost-Free Period and the Number of Frost Days across China under Climate Change Using ERA5-Land Reanalysis Dataset. *Remote Sens.* 2022, 14, 2400. <https://doi.org/10.3390/rs14102400>.

Li, Z.Q., Xie, Y., Hou, W., Liu, Z., Bai, Z., Hong, J., Ma, Y., Huang, H. Lei, X., Sun, X., Liu, X., Yang, B., Qiao, Y., Zhu, J., Cong, Q., Zheng, Y., Song, M., Zou, P., Hu, Z., Lin, J., Fan, L., 2022b. In-Orbit Test of the Polarized Scanning Atmospheric Corrector (PSAC) Onboard Chinese Environmental Protection and Disaster Monitoring Satellite Constellation HJ-2 A/B. *IEEE Transactions on Geoscience and Remote Sensing*, vol. 60, pp. 1-17, Art no. 4108217, doi: 10.1109/TGRS.2022.3176978.

Li, Z., Hou, W., Hong, J., Fan, C., Wei, Y., Liu, Z., Lei, X., Qiao, Y., Hasekamp, O. P., Fu, G., Wang, J., Dubovik, O., Qie, L. Zhang, Y., Xua, H., Xie, Y., Song, M., Zou, P., Luo, D., Wang, Y., Tu, B., 2022c. The polarization crossfire (PCF) sensor suite focusing on satellite remote sensing of fine particulate matter PM<sub>2.5</sub> from space, *Journal of Quantitative Spectroscopy & Radiative Transfer* 286, 108217, <https://doi.org/10.1016/j.jqsrt.2022.108217>.

Li, X., Cohen, J. B., Qin, K., Geng, H., Wu, X., Wu, L., Yang, C., Zhang, R., Zhang, L. 2023. Remotely sensed and surface measurement- derived mass-conserving inversion of daily NO<sub>x</sub> emissions and inferred combustion technologies in energy-rich northern China. *Atmospheric Chemistry and Physics*, 23(14), 8001–8019. <https://doi.org/10.5194/acp-23-8001-2023>.

Liu, Y., Lin, T., Hong, J., Wang, Y., Shi, L., Huang, Y., Wu, X., Zhou, H., Zhang, J., de Leeuw, G., 2021. Multi-dimensional satellite observations of aerosol properties and aerosol types over three major urban

clusters in eastern China, *Atmos. Chem. Phys.*, 21, 12331–12358, <https://doi.org/10.5194/acp-21-12331-2021>, 2021.

Liu, J., Cohen, J. B., He, Q., Tiwari, P., Qin, K. 2024. Accounting for NO<sub>x</sub> emissions from biomass burning and urbanization doubles existing inventories over South, Southeast and East Asia. *Communications Earth & Environment*, 5(1), 1–16. <https://doi.org/10.1038/s43247-024-01424-5>.

Lorente, A., Boersma, K.F., Eskes, H.J., Veefkind, J.P., van Geffen, J.H.G.M., de Zeeuw, M.B., Denier van der Gon, H.A.C., Beirle, S., Krol, M.C., 2019. Quantification of nitrogen oxides emissions from build-up of pollution over Paris with TROPOMI. *Sci. Rep.* 9, 20033. <https://doi.org/10.1038/s41598-019-56428-5>.

Lyapustin, A., Wang, Y., Korkin, S., Huang, D., 2018. MODIS Collection 6 MAIAC algorithm. *Atmos. Meas. Tech.*, 11, 5741–5765, <https://doi.org/10.5194/amt-11-5741-2018>.

Manisalidis, I., Stavropoulou, E., Stavropoulos, A., Bezirtzoglou, E., 2020. Environmental and Health Impacts of Air Pollution: A Review. *Front. Public Health* 8:14. doi: 10.3389/fpubh.2020.00014.

MEE, 2024. Ministry of Ecology and Environment of the People's Republic of China <https://www.mee.gov.cn/> (last accessed: 30 June 2024).

MEIC, 2024. Multi-resolution Emission Inventory model for Climate and air pollution research. <http://meicmodel.org/> (last accessed: 30 June 2024).

Neale, R. B., Gettelman, A., Park, S., Chen, C. -C., Lauritzen, P. H., Williamson, D. L., Conley, A.J., Kinnison, D., Marsh, D., Smith, A.K., Vitt, F.M., Garcia, R., Lamarque, J.-F., Mills, M.J., Tilmes, S., Morrison, H., Cameron-Smith, P., Collins, W.D., Iacono, M.J., Easter, R.C., Liu, X., Ghan, S.J., Rasch, P.J., Taylor, M. A., 2012. Description of the NCAR Community Atmosphere Model (CAM 5.0) (No. NCAR/TN-486+STR). doi:10.5065/wgtk-4g06.

Neuman, J. A., 2003. Variability in ammonium nitrate formation and nitric acid depletion with altitude and location over California, *J. Geophys. Res.*, 108, 4557, <https://doi.org/10.1029/2003jd003616>.

Qin, K., Lu, L., Liu, J., He, Q., Shi, J., Deng, W., Wang, S., Cohen, J. B. 2023. Model-free daily inversion of NO<sub>x</sub> emissions using TROPOMI (MCMFE-NO<sub>x</sub>) and its uncertainty: Declining regulated emissions and growth of new sources. *Remote Sensing of Environment*, 295, 113720. <https://doi.org/10.1016/j.rse.2023.113720>

Rao, N.V., Rajasekhar, M., Chinna Rao, G., 2014. Detrimental effect of Air pollution, Corrosion on Building Materials and Historical Structures. *American Journal of Engineering Research (AJER)*, Volume-03, Issue-03, pp-359-364. (e-ISSN : 2320-0847 p-ISSN : 2320-0936).

Reitebuch, O., 2012. The Spaceborne Wind Lidar Mission ADM-Aeolus, in: *Atmospheric physics: Background, methods, trends*, edited by: Schumann, U., *Research Topics in Aerospace*, Springer, Berlin, London, 815–827, 2012.

Rienecker, M.M., Suarez, M.J., Gelaro, R., Todling, R., Bacmeister, J., Liu, E., Bosilovich, M.G., Schubert, S.D., Takacs, L., Kim, G., Bloom, S., Chen, J., Collins, D., Conaty, A., da Silva, A., Gu, W., Joiner, J., Koster, R.D., Lucchesi, R., Molod, A., Owens, T., Pawson, S., Pegion, P., Redder, C.R., Reichle, R., Robertson, F.R., Ruddick, A.G., Sienkiewicz, M., Woollen, J., 2011. MERRA: NASA's Modern-Era Retrospective Analysis for Research and Applications. *Journal of Climate*, 24(14), 3624-3648, <https://doi.org/10.1175/JCLI-D-11-00015.1>.

Sluis, W.W., Allaart, M.A.F., Piters, A.J.M., Gast, L.F.L., 2010. The development of a nitrogen dioxide sonde, *Atmos. Meas. Tech.*, 3, 1753–1762, <https://doi.org/10.5194/amt-3-1753-2010>.

Sogacheva, L., Rodriguez, E., Kolmonen, P., Virtanen, T. H., Saponaro, G., de Leeuw, G., Georgoulas, A. K., Alexandri, G., Kourtidis, K., van der A, R. J., 2018. Spatial and seasonal variations of aerosols over

China from two decades of multi-satellite observations – Part 2: AOD time series for 1995–2017 combined from ATSR ADV and MODIS C6.1 and AOD tendency estimations, *Atmos. Chem. Phys.*, 18, 16631–16652, <https://doi.org/10.5194/acp-18-16631-2018>.

Sogacheva, L., Popp, T., Sayer, A. M., Dubovik, O., Garay, M. J., Heckel, A., Hsu, N. C., Jethva, H., Kahn, R. A., Kolmonen, P., Kosmale, M., de Leeuw, G., Levy, R. C., Litvinov, P., Lyapustin, A., North, P., Torres, O., Arola, A., 2020. Merging regional and global aerosol optical depth records from major available satellite products, *Atmos. Chem. Phys.*, 20, 2031–2056, <https://doi.org/10.5194/acp-20-2031-2020>.

Sun, K., Chen, X., Zhu, Z., Zhang, T., 2017. High Resolution Aerosol Optical Depth Retrieval Using Gaofen-1 WFV Camera Data. *Remote Sens.* 2017, 9, 89; doi:10.3390/rs9010089.

S5P-PAL Data Portal, 2024. <https://data-portal.s5p-pal.com/> (last accessed 30 June 2024).

TEMIS, 2024. TROPOMI NO<sub>2</sub> data version overview.

[https://www.temis.nl/airpollution/no2col/tropomi\\_no2\\_data\\_versions.php](https://www.temis.nl/airpollution/no2col/tropomi_no2_data_versions.php). (last accessed: 30 June 2024).

TEMPO, 2024. Tropospheric Emissions: Monitoring of Pollution. <https://tempo.si.edu/> (last accessed 30 June 2024).

van der A, R.J., Mijling, B., Ding, J., Koukouli, M.E., Liu, F., Li, Q., Mao, H., Theys, N., 2017. Cleaning up the air: effectiveness of air quality policy for SO<sub>2</sub> and NO<sub>x</sub> emissions in China, *Atmos. Chem. Phys.* 17, 1775–1789. <https://doi.org/10.5194/acp17-1775-2017>.

Varotsos, C.A., Zellner, R., 2010. A new modeling tool for the diffusion of gases in ice or amorphous binary mixture in the polar stratosphere and the upper troposphere, *Atmos. Chem. Phys.*, 10, 3099–3105, <https://doi.org/10.5194/acp-10-3099-2010>.

Varotsos, C.A., Ghosh, S., 2017. Impacts of climate warming on atmospheric phase transition mechanisms. *Theoretical and Applied Climatology*, 130(3-4), 1111–1122, <https://doi.org/10.1007/s00704-016-1951-2>.

Varotsos, C.; Tzani, C.; Cracknell, A., 2009. The enhanced deterioration of the cultural heritage monuments due to air pollution. *Environ. Sci. Pollut. Res. Int.* 2009, 16, 590–592, doi:10.1007/s11356-009-0114-8.

Wang, H., He, S., 2015. The North China/Northeastern Asia Severe Summer Drought in 2014. *J. Climate* 28, 6667. DOI: 10.1175/JCLI-D-15-0202.1

Wang, Y., Dörner, S., Donner, S., Böhnke, S., De Smedt, I., Dickerson, R. R., Dong, Z., He, H., Li, Z., Li, Z., Li, D., Liu, D., Ren, X., Theys, N., Wang, Y., Wang, Y., Wang, Z., Xu, H., Xu, J., Wagner, T., 2019. Vertical profiles of NO<sub>2</sub>, SO<sub>2</sub>, HONO, HCHO, CHOCHO and aerosols derived from MAX-DOAS measurements at a rural site in the central western North China Plain and their relation to emission sources and effects of regional transport, *Atmos. Chem. Phys.*, 19, 5417–5449, <https://doi.org/10.5194/acp-19-5417-2019>.

Wang, W., van der A, R., Ding, J., van Weele, M., Cheng, T., 2021. Spatial and temporal changes of the ozone sensitivity in China based on satellite and ground-based observations, *Atmos. Chem. Phys.*, 21, 7253–7269, <https://doi.org/10.5194/acp-21-7253-2021>.

WAQI, 2024. World's Air Pollution: Real-time Air Quality Index. 2024. <https://waqi.info/> (last accessed 30 June 2024).

WHO, 2024. World Health Organization Global Air Quality Guidelines, <https://www.who.int/news-room/questions-and-answers/item/who-global-air-quality-guidelines> (last accessed 30 June 2024).

WMO, 2024. <https://space.oscar.wmo.int/instruments/view/gems> (last accessed 30 June 2024).

- Xia, X., Zhang, K., Yang, R., Zhang, Y., Xu, D., Bai, K., Guo, J., 2022. Impact of near-surface turbulence on PM<sub>2.5</sub> concentration in Chengdu during the COVID-19 pandemic. *Atmospheric Environment*, 268, 118848. <https://doi.org/10.1016/j.atmosenv.2021.118848>.
- Xiao, Q., Zheng, Y., Geng, G., Chen, C., Huang, X., Che, H., Zhang, X., He, K., Zhang, Q., 2021. Separating emission and meteorological contributions to long-term PM<sub>2.5</sub> trends over eastern China during 2000–2018. *Atmos. Chem. Phys.*, 21, 9475–9496, <https://doi.org/10.5194/acp-21-9475-2021>.
- Xu, J., Han, F., Li, M., Zhang, Z., Xiaohui, D., Wei, P., 2019. On the opposite seasonality of MODIS AOD and surface PM<sub>2.5</sub> over the Northern China plain. *Atmospheric Environment*, Volume 215, 116909, <https://doi.org/10.1016/j.atmosenv.2019.116909>.
- Xue, Y.; He, X.W.; Xu, H.; Guang, J.; Guo, J.P.; Mei, L.L., 2014. China Collection 2.0: The aerosol optical depth dataset from the synergetic retrieval of aerosol properties algorithm. *Atmos. Environ.* 2014, 95, 45–58. <https://doi.org/10.1016/j.atmosenv.2014.06.019>.
- Xue, Y.; Li, Y.; Guang, J.; Tugui, A.; She, L.; Qin, K.; Fan, C.; Che, Y.; Xie, Y.; Wen, Y., Wang, Z., 2020. Hourly PM<sub>2.5</sub> Estimation over Central and Eastern China Based on Himawari-8 Data. *Remote Sensing* 2020, 12, 855 (15 pp), <https://doi.org/10.3390/rs12050855>.
- Yin, Z., Wang, H., and Chen, H.: Understanding severe winter haze events in the North China Plain in 2014: roles of climate anomalies, *Atmos. Chem. Phys.*, 17, 1641–1651, <https://doi.org/10.5194/acp-17-1641-2017>, 2017.
- Yin, Y. Ke, Tu, Y., Wang, X., Chen, Y., Jiao, S., 2024. Changes of summer meteorological drought and their relationship with the dry and wet circulation patterns in the Huai River basin, China. *Journal of Hydrology: Regional Studies* 52, 101710, <https://doi.org/10.1016/j.ejrh.2024.101710>
- Yuan, G., Yang, W., 2019. Evaluating China's Air Pollution Control Policy with Extended AQI Indicator System: Example of the Beijing-Tianjin-Hebei Region, *Sustainability*, 11, 939, <https://doi.org/10.3390/su11030939>.
- Zhai, S., Jacob, D.J., Wang, X., Shen, L., Li, K., Zhang, Y., Gui, K., Zhao, T., Liao, H., 2019. Fine particulate matter (PM<sub>2.5</sub>) trends in China, 2013–2018: separating contributions from anthropogenic emissions and meteorology. *Atmos. Chem. Phys.*, 19, 11031–11041, <https://doi.org/10.5194/acp-19-11031-2019>.
- Zhang, Y., Li, Z Q., 2015. Remote sensing of atmospheric fine particulate matter (PM<sub>2.5</sub>) mass concentration near the ground from satellite observation. *Remote Sensing of Environment*, 160, 252-262, <https://doi.org/10.1016/j.rse.2015.02.005>.
- Zhang, Y., Li, Z., Zhang, Y., Li, D., Qie, L., Che, H., Xu, H., 2017. Estimation of aerosol complex refractive indices for both fine and coarse modes simultaneously based on AERONET remote sensing products, *Atmos. Meas. Tech.*, 10, 3203–3213, <https://doi.org/10.5194/amt-10-3203-2017>, 2017.
- Zhang, Q., Zheng, Y., Tong, D., Shao, M., Wang, S., Zhang, Y., Xu, X., Wang, J., He, H., Liu, W., Ding, Y., Lei, Y., Li, J., Wang, Z., Zhang, X., Wang, Y., Cheng, J., Liu, Y., Shi, Q., Yan, L., Geng, G., Hong, C., Li, M., Liu, F., Zheng, B., Cao, J., Ding, A., Gao, J., Fu, Q., Huo, J., Liu, B., Liu, Z., Yang, F., He, K., Hao, J., 2019a. Drivers of improved PM<sub>2.5</sub> air quality in China from 2013 to 2017. *PNAS*, 116, 49, 24463–24469, <https://doi.org/10.1073/pnas.1907956116>.
- Zhang X., Xu, X., Ding, Y., Liu, Y., Zhang, H., Wang, Y., Zhong, J., 2019b. The impact of meteorological changes from 2013 to 2017 on PM<sub>2.5</sub> mass reduction in key regions in China. *Sci. China Earth Sci.*, 62, 1885–1902, <https://doi.org/10.1007/s11430-019-9343-3>.

Zhang, Y, Li, Z., Chang, W., Zhang, Y., de Leeuw, G., Schauer, J.J., 2020. Satellite Observations of PM<sub>2.5</sub> Changes and Driving Factors based Forecasting over China 2000-2025. *Remote Sensing* 2020, 12, 2518; doi:10.3390/rs12162518.

Zhang, X., van der A, R., Ding, J., Eskes, H., van Geffen, J., Yin, Y., Anema, J., Vagasky, C., Lapierre, J.L., Kuang, X., 2023a. Spaceborne Observations of Lightning NO<sub>2</sub> in the Arctic. *Environ. Sci. Technol.* 2023, 57, 6, 2322–2332, <https://doi.org/10.1021/acs.est.2c07988>.

Zhang, X., van der A, R., Ding, J., Zhang, X., Yin, Y., 2023b. Significant contribution of inland ships to the total NO<sub>x</sub> emissions along the Yangtze River, *Atmos. Chem. Phys.*, 23, 5587–5604, <https://doi.org/10.5194/acp-23-5587-2023>, 2023.

Zhang, Q., Boersma, K.F., Zhao, B., Eskes, H., Chen, C., Zheng, H., Zhang, X., 2023c. Quantifying daily NO<sub>x</sub> and CO<sub>2</sub> emissions from Wuhan using satellite observations from TROPOMI and OCO-2, *Atmos. Chem. Phys.*, 23, 551–563, <https://doi.org/10.5194/acp-23-551-2023>.

Zeng, H., Xiao, C., Chen, X., Ye, D., 2019. State of China's climate in 2018. *Atmospheric and Oceanic Science Letters*, 12:5, 349-354, DOI:10.1080/16742834.2019.1632147.

Zeng, H., Xiao, C., Chen, X., Ye, D., 2020. State of China's climate in 2019, *Atmospheric and Oceanic Science Letters*, 13:4, 356-362, DOI:10.1080/16742834.2020.1762159.

Zheng, B., Tong, D., Li, M., Liu, F., Hong, C., Geng, G., Li, H., Li, X., Peng, L., Qi, J., Yan, L., Zhang, Y., Zhao, H., Zheng, Y., He, K., Zhang, Q., 2018a. Trends in China's anthropogenic emissions since 2010 as the consequence of clean air actions, *Atmos. Chem. Phys.*, 18, 14095–14111, <https://doi.org/10.5194/acp-18-14095-2018>.

Zheng, B., Chevallier, F., Ciais, P., Yin, Y., Deeter, M., Worden, H., Wang, Y., Zhang, Q., He, K., 2018b. Rapid decline in carbon monoxide emissions and export from East Asia between years 2005 and 2016. *Environmental Research Letters*. 13. 10.1088/1748-9326/aab2b3.

Zhou, Y., Guo, J., Zhao, T., Lv, J., Bai, Y., Wang, C., Sun, X., Hu, W., 2022. Roles of atmospheric turbulence and stratification in a regional pollution transport event in the middle reaches of the Yangtze River. *Earth and Space Science*, 9, e2021EA002062. <https://doi.org/10.1029/2021EA002062>

#### Appendix: List of abbreviations

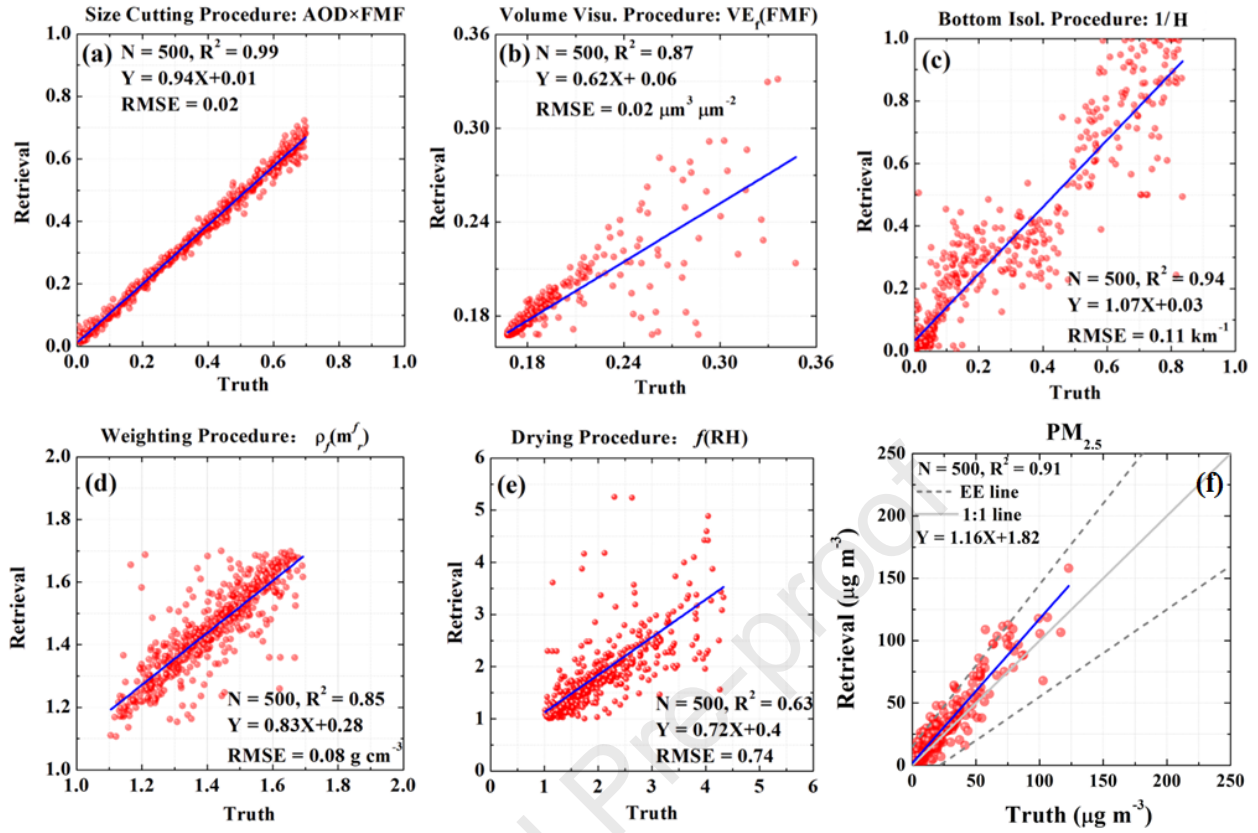
AEOLUS	Atmospheric Dynamics Mission-Aeolus (ADM-Aeolus)
AERONET	Aerosol Robotic Network
AHI	Advanced Himawari Imager
AIS	Automatic Identification System
ALADIN	Atmospheric Laser Doppler Instrument
ALH	Aerosol Layer Height
AOD	Aerosol Optical Depth
AQ	Air Quality
AQI	Air Quality Index
ATSR-2	Along Track Scanning Radiometer 2

BC	Black Carbon
BVOC	Biogenic volatile organic compounds
CAM5	Community Atmospheric Model version 5
CCD	Charge Coupled Device
CCS	China Classification Society
CESM	Community Earth System Model
CHCO	Formaldehyde
CHEOS	civilian China High-Resolution Earth Observation System
CNEMC	China National Environmental Monitoring Center
CO	Carbon Monoxide
COTC	Carbon monoxide total column
CS	Condensation Sink
D	Diffusion coefficient
DECISO	Daily Emissions Constrained by Satellite Observations
E	Activation Energy
ECV	Essential Climate Variables
EE	Expected Error
EMBE	empirical model for BVOC emissions
EMPAC	Exploitation of satellite remote sensing to enhance our comprehension of the Mechanisms and Processes influencing Air quality in China
ENVISAT	Environmental Satellite
EPA	United States Environmental Protection Agency
ESA	European Space Agency
EUMETSAT	European Organisation for the Exploitation of Meteorological Satellites
FMF	Fine Mode Fraction
f(RH)	Hygroscopic Growth Factor
GF-1	Gaofen-1
GCOS	Global Climate Observing System
GEMS	Geostationary Environment Monitoring Spectrometer
GEO	Geostationary Earth Orbit

GLD360	Global Lightning Dataset 360
HIS	Hyperspectral Imager
HLOS	Horizontal Line of Sight
HNB	Hunan and Hubei
H8	Himawari-8 (JMA)
JMA	Japan Meteorological Agency
IASI	Infrared Atmospheric Sounding Interferometer
IR	Infra-Red
IRS	Infrared Spectroradiometer
KNMI	Royal Netherlands Meteorological Institute
$k_B$	Boltzmann constant
LEO	Low Earth Orbit
LNO <sub>2</sub>	Lightning NO <sub>2</sub>
MAIAC	Multi-Angle Implementation of Atmospheric Correction
MAX-DOAS	Multi-AXis Differential Optical Absorption Spectroscopy
MEE	Ministry of Ecology and Environment
MEIC	Multi-resolution Emission Inventory for China
MERRA-2	Modern Era Retrospective analysis for Research and Applications, version 2
METOP	METEorological Operational satellite
MIR	Mid Infra-Red
MODIS	Moderate Resolution Imaging Spectroradiometer
MOST	Ministry of Science and Technology of the P.R. China
MTG-S	Meteosat Third Generation Sounder
$m_r^f$	real part of the complex refractive index of dry fine mode particles
NASA	United States National Aeronautics and Space Administration
NCP	North China Plain
NH <sub>3</sub>	Ammonia
NIR	Near Infra-red
NO	Nitrogen Monoxide
NO <sub>2</sub>	Nitrogen Dioxide

NO <sub>x</sub>	NO + NO <sub>2</sub>
NRSCC	National Remote Sensing Center
NUIST	Nanjing University of Information Science and Technology
OCO-2	Orbiting Carbon Observatory-2
OMI	Ozone Monitoring Instrument
ORG	Organic Precursor Vapor Concentration
O <sub>3</sub>	Ozone
PAR	photosynthetically active radiation
PBL	Planetary Boundary Layer
PBLH	Planetary Boundary Layer Height
PCF	Polarization CrossFire
p <sub>E</sub>	water vapor pressure
PM	Particulate matter
PMRS	Particulate Matter Remote Sensing
PM2.5/PM10	Mass concentration of particles smaller than 2.5 μm (PM2.5) or 10 μm (PM10)
PRD	Pearl River Delta
PSAC	Polarized Scanning Atmospheric Corrector
Q	global solar radiation
RH	Relative Humidity
RWP	Radar Wind Profiler
S	diffuse solar radiation
SCB	Sichuan Basin
SECBH	South-Eastern China Below the Hu line
SEIM	Shipping Emission Inventory Model
SNR	Signal to Noise Ratio
SONET	Sun-sky radiometer Observation NETWORK
SO <sub>2</sub>	Sulfur Dioxide
SRAP	Synergetic Retrieval of Aerosol Properties
TEI	Thermo Environmental Instruments
TEMPO	Tropospheric Emissions: Monitoring of Pollution

TOA	Top of Atmosphere
TROPOMI	TROPOspheric Monitoring Instrument
TrO <sub>3</sub>	Tropospheric O <sub>3</sub>
UAV	Unmanned Aerial Vehicle
UV	Ultra-Violet Radiation
VCD	Vertical Column Density
VE <sub>f</sub>	Fine-mode columnar volume-to-extinction ratio
VIS	Visible
VOC	Volatile organic compounds
WAQI	World Air Quality Index
WFV	Wide-Field-of-View
WHO	World Health Organization
WMO	World Meteorological Organization
YRD	Yangtze River Delta
$\rho_f$	effective density of fine-mode aerosol particles
$\tau_a$	AERONET AOD



**Highlights**

- AOD, NO<sub>2</sub> and CO time series show effectiveness emission reduction policy in China;
- Meteorological effects influence the aerosol concentration trends.
- Production of NO<sub>2</sub> from lightning important in the Arctic region;
- Improved superposition model to quantify city-scale emissions of NO<sub>x</sub> and CO<sub>2</sub>;
- High-resolution NO<sub>x</sub> emission data base over the Yangtze River Delta from TROPOMI;
- Estimate of impact of inland ship emissions on air quality in Nanjing region.

Journal Pre-proof

**Declaration of interests**

The authors declare that they have no known competing financial interests or personal relationships that could have appeared to influence the work reported in this paper.

The authors declare the following financial interests/personal relationships which may be considered as potential competing interests:

Journal Pre-proof